

<sup>a</sup>A. R. Páramo, <sup>a,b</sup>F. Sordo, <sup>a</sup>D. Garoz, <sup>c</sup>B. Le-Garrec, <sup>c</sup>J.M. Perlado, <sup>c</sup>A. Rivera

<sup>a</sup> Instituto de Fusión Nuclear - UPM. c/ José Gutiérrez Abascal, 2 - 28006 Madrid, Spain  
(angel.rodriquez.paramo@upm.es)

<sup>b</sup> ESS-Bilbao. Edificio Cosimet. Paseo Landabbarri, 2 1ª planta - 48940 Leioa, Spain

<sup>c</sup> Institute of Physics, Academy of Sciences, Prague, Czech Republic

## Abstract

The development and fabrication of final focusing components is one of the technological developments needed to build a laser fusion power plant. These components are key elements for the plant operation as because the target compression and ignition depends on the laser power delivery through the final focusing components. Final focusing components face hostile irradiation conditions which hinder its operation.

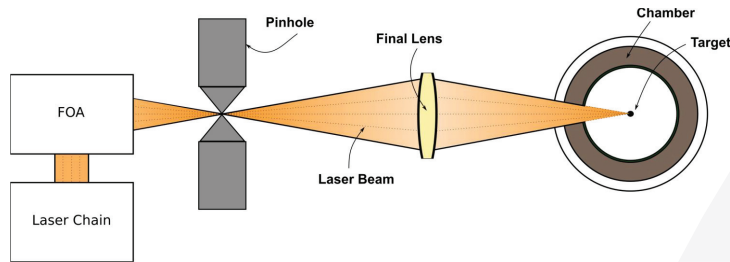
We have developed a conceptual design of final focusing components based on silica transmission lenses. Neutron irradiation will lead to a non-uniform steady state temperature profile along the final lenses leading to aberrations. A temperature control system is necessary to correct these effects. Our design is based on a heat transfer fluid that keeps the temperature profile smooth and constant in all the operation phases.

## Introduction

In this work [1], we study the dependence of the lens focusing on temperature, both during the start-up and normal operation.

The solution adopted in HiPER [2] for the final optical assembly (FOA) is a scheme with 48 laser beams using. Different laser beamlets are used for the different stages of ignition (foot, compression and shock) to obtain a zooming effect [3]. In order to adapt for the different beamlets the final lens is divided 4 x 4 quadrangles.

We study the aberrations in the focal spot through the illumination uniformity level ( $\sigma$ ) and efficiency( $\eta$ ). To guarantee that the illumination uniformity is suitable for ignition  $\sigma$  should be kept below 1 % with  $\eta > 90$  %

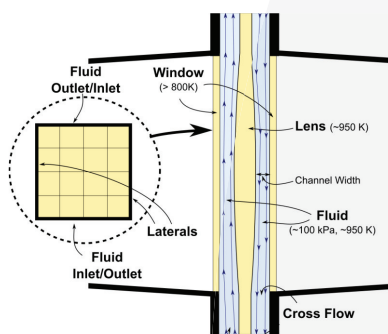


## Proposal of Temperature Control System

In order to fulfil the temperature requirements for the HiPER silica transmission final lenses, a temperature control system must be designed. We chose a temperature control system based on a heat-transfer fluid.

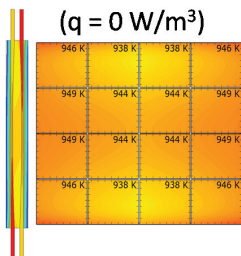
For the design of the system we have studied the flow pattern (counter-flow), the fluid pressure (100 kPa), pressure drop (1 kPa), windows thickness, gas formation and retention, possible fluids, optimal channel width and operational regimes (start-up and normal,).

We conclude that operation would be possible using He or CO<sub>2</sub> with channel widths larger than ~ 6 mm.



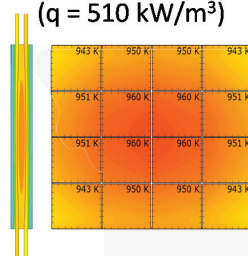
### Start-up

( $q = 0 \text{ W/m}^3$ )



### Normal

( $q = 510 \text{ kW/m}^3$ )

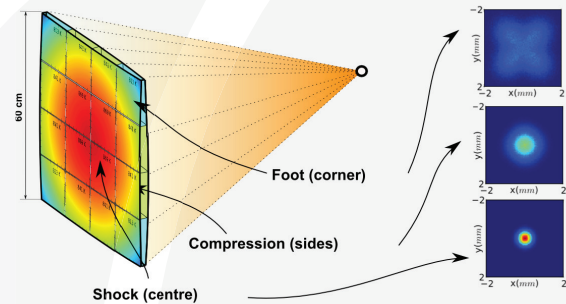


Fluid	Design T <sub>0</sub> (K)	Operation Regime	Fluid T <sub>1</sub> (K)	Foot	$\eta$ Comp.	Shock	Foot	$\sigma$ Comp.	Shock
He	947	Start-up	985	92%	92%	92%	0.17%	0.18%	0.46%
		Normal	950	92%	92%	89%	0.16%	0.23%	0.46%
CO <sub>2</sub>	943	Start-up	995	92%	92%	92%	0.19%	0.18%	0.18%
		Normal	950	92%	92%	87%	0.17%	0.28%	0.29%

## Temperature Requirements for the Lens

The temperature of the lenses has to be controlled for the correct focusing of laser beamlets:

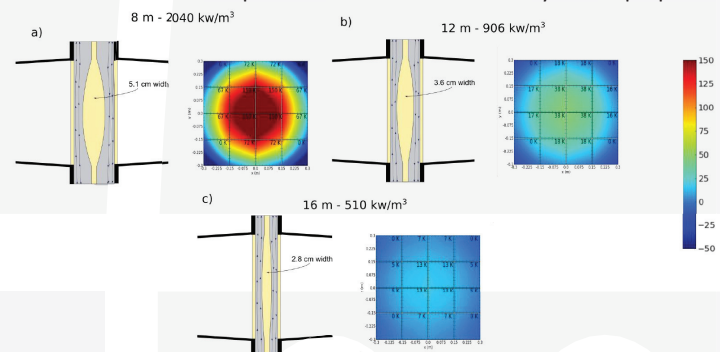
- **Temperature limits:** higher than 800 K to anneal colour centres from neutron irradiation [4-6] and below 1223 K to avoid mechanical failure [7].
- **Constant temperature:** during the start-up, partial regime or normal operation, only a small temperature deviation (~20 K) is acceptable.
- **Uniform temperature:** due to the lens profile (thicker at its centre) a temperature profile appears, that causes optical aberrations.



## Lens Distance to Target

Finally we study if the distance from the target could be reduced from our base scenario of 16 m. Placing the lens at 12 m we observe how the temperature variation increases, however with an adequate control operation could be possible. Placing the lenses nearer (8 m) would not be possible as the temperature variation is too high.

Summarizing, a pre-commercial scenario for the HiPER project has been studied. In this scenario final lenses must be placed at a distance of ~ 16 m, in order to control the temperature a heat-transfer fluid system is proposed.



## References

- [1] Páramo A. R. et al., Nucl. Fusion 54 123019, 2014
- [2] Le Garrec B. et al., Proc. SPIE 8080 80801V, 2011.
- [3] Canaud B. and Garaude F., Nucl. Fusion 45 L43, 2005.
- [4] Páramo A. R. et al., J. Nucl. Mater. 444 46974, 2014
- [5] Marshall C.D. et al., J. Non-Cryst. Solids 212 5973, 1997
- [6] Latkowski J.F. et al., Fusion Sci. Technol. 43 54058, 2003
- [7] Heraeus Quarzglas Quartz Glass for Optics: Data and Properties

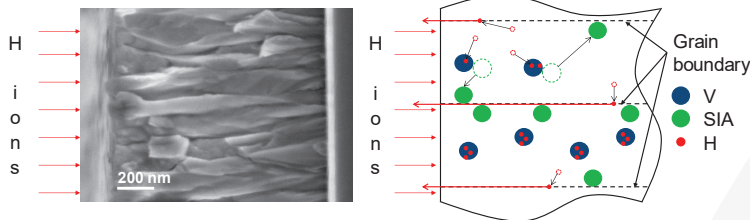
\* The illumination uniformity level ( $\sigma$ ) is defined as the laser intensity root mean deviation. The efficiency ( $\eta$ ) is defined as the ratio of power deposited in the target to the laser power.

## Abstract

The influence of grain boundaries (GBs) on the radiation-induced defects evolution as well as on hydrogen (H) retention in nanostructured tungsten (W) at 300 K were studied by computer simulation. Nanostructured tungsten was implanted with hydrogen and carbon (C), at energies of 170 keV and 665 keV respectively. Three different irradiation conditions were studied: (i) H single implantation, (ii) C and H co-implantation and (iii) C and H sequential implantation. Computer simulations were performed with the MMonCa code, based on Object Kinetic Monte Carlo (OKMC) technique. The results show that GBs have a clear influence on the amount of vacancies. H retention is highly influenced by both the GBs themselves and the vacancy concentration. H is retained in monovacancies, in the great majority. From the comparison between the computational results and the experimental ones, it can be inferred that GBs act as preferential paths for H diffusion.

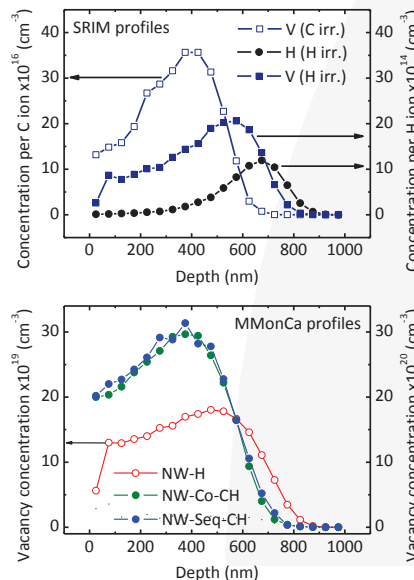
## Introduction

- Tungsten is proposed as first wall material in Inertial Fusion Confinement (IFC) reactors due to its good refractory properties, low activation rate and low tritium retention
- However, W will be irradiated by H ions at energies high enough to produce Frenkel pairs (FPs)
- H is retained in vacancies (Vs), which may grow into bubbles causing surface blistering and exfoliation
- Nanostructured W is being investigated due to its influence on the distribution of both FP and H atoms [1] and its „self-healing” behaviour



## Results

- SRIM calculates V and H profiles due to C and H irradiation. Clear vacancy concentration peaks are observed
- C produces 365 Vs per C ion
- H produces 2.3 Vs per H ion
- Almost no V production at depths higher than 800 nm
- MMonCa takes into account annihilation between Vs and self-interstitial atoms (Is)
- V concentration peaks are smoother than those calculated by SRIM
- In NW-H case, the peak is far less pronounced



## Conclusions

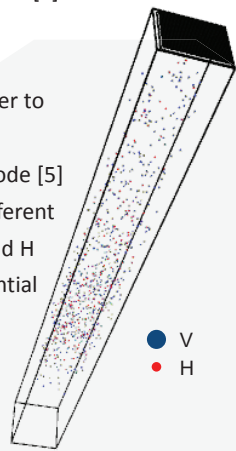
- Regarding the H retention, our simulations are in very good agreement with the experimental results: not only the total H concentration but also H distribution in depth
- GBs have a clear influence on FP annihilation and on H concentration
- From the comparison between experimental and OKMC results, it can be inferred that GBs act as preferential paths for H diffusion

## Acknowledgements

Part of the work was financed by MINECO (Spain) under the projects RADIAFUS ENE-2012-39787-CO6, MATFUSLA AIC-A-2011-0718 and by the EUROfusion Consortium under the project AWP15-ENR-01/CEA-02. Authors acknowledge Ramón y Cajal Fellowship (RyC-2012-10639), Junta de Andalucía and the European Commission (the 7<sup>th</sup> Framework co-funding)

## Object Kinetic Monte Carlo (OKMC)

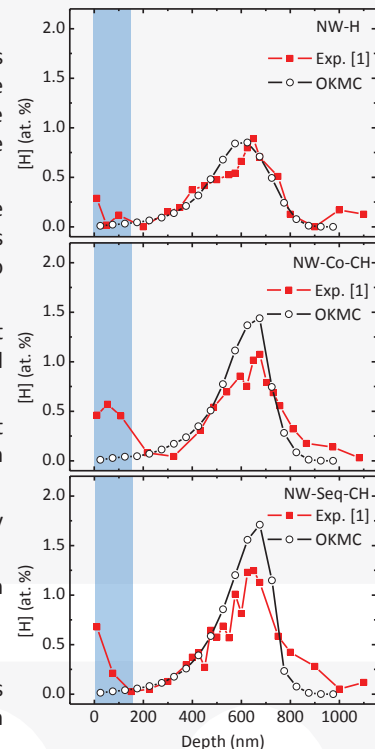
- Simulations were performed with the MMonCa code [2]
- MMonCa was parameterized with in-house DFT data [3] as well as with values from Literature [4]
- Simulation box:  $50 \times 50 \times 1000 \text{ nm}^3$
- The four lateral surfaces act as perfect sinks, in order to simulate the effect of GBs on defects and H atoms
- Damage cascades were calculated with the SRIM code [5]
- C (665 keV) and H (170 keV) irradiation in three different conditions: (i) H single implantation (NW-H), (ii) C and H co-implantation (NW-Co-CH) and (iii) C and H sequential implantation (NW-Seq-CH)
- C and H flux:  $2.78 \times 10^{12} \text{ cm}^{-2} \text{ s}^{-1}$
- C and H fluence:  $5 \times 10^{16} \text{ cm}^{-2}$
- Temperature: 300 K
- Irradiation time: 5 h



- The region between 0-150 nm was not considered in the results. The high H retention observed in the experiments is related to surface contamination [1]
- Only defects in the interior of the grain are considered. Thus, defects trapped at GBs are not taken into account in the results
- There is a very good agreement between OKMC and experimental results
- Vacancies cannot migrate in W at 300 K due to their large migration energy ( $E_m(V) = 1.66 \text{ eV}$ ) [4]
- Self-interstitial atoms migrate very fast to the GBs ( $E_m(I) = 0.013 \text{ eV}$ ) [4]
- H atoms are retained in monovacancies, in the great majority
- Clusters up to  $H_6V_1$  are observed
- The total H concentration is approximately the same in both experiments and OKMC results

## References

- [1] Gonzalez-Arrabal *et al.* J. Nucl. Mater. 453 (2014) 287-295
- [2] Martín-Bragado *et al.* Comput. Phys. Commun. 184 (2013) 2703
- [3] C. González *et al.* Nucl. Fusion 55 (2015) 113009
- [4] Becquart *et al.* J. Nucl. Mater. 403 (2010) 75-88
- [5] Ziegler *et al.* Nucl. Instrum. Methods. Phys. Res. Sect. B Beam Interact. Mater. At. 268 (2010) 1818-1823





# Hydrogen retention in nanostructured tungsten as compared with coarse grained tungsten

<sup>a</sup>M. Panizo-Laiz, <sup>a</sup>R. González-Arrabal, <sup>a</sup>N. Gordillo, <sup>b</sup>E. Tejado, <sup>c</sup>F. Munnik, <sup>a</sup>A. Rivera, <sup>a</sup>J. M. Perlado

<sup>a</sup>Instituto de Fusión Nuclear, UPM, Madrid, Spain (miguel.panizo.laiz@Gmail.com)

<sup>b</sup>Departamento de Ciencia de Materiales, ETSI Caminos, Canales y Puertos, UPM, Madrid, Spain

<sup>c</sup>Helmholtz-Zentrum Dresden-Rossendorf, Dresden, Germany

## Abstract

The lack of plasma facing materials (PFM) able to withstand the severe radiation conditions expected in fusion reactors is the actual bottle neck for fusion to become a reality. Nowadays W is one of the most promising options for PFM in a fusion reactor. However, some limitations such as the light species retention have been found for standard coarse-grain W (CGW).

**Nanostructured materials (NM) have demonstrated to present a higher radiation and swelling resistant due to the influence of the grain boundaries in the:**

- Radiation-induced damage  $\Rightarrow$  Self-healing behaviour.
- Light species retention  $\Rightarrow$  Light species are pinned at the grain boundaries (GB) and they act as effective diffusion channels.

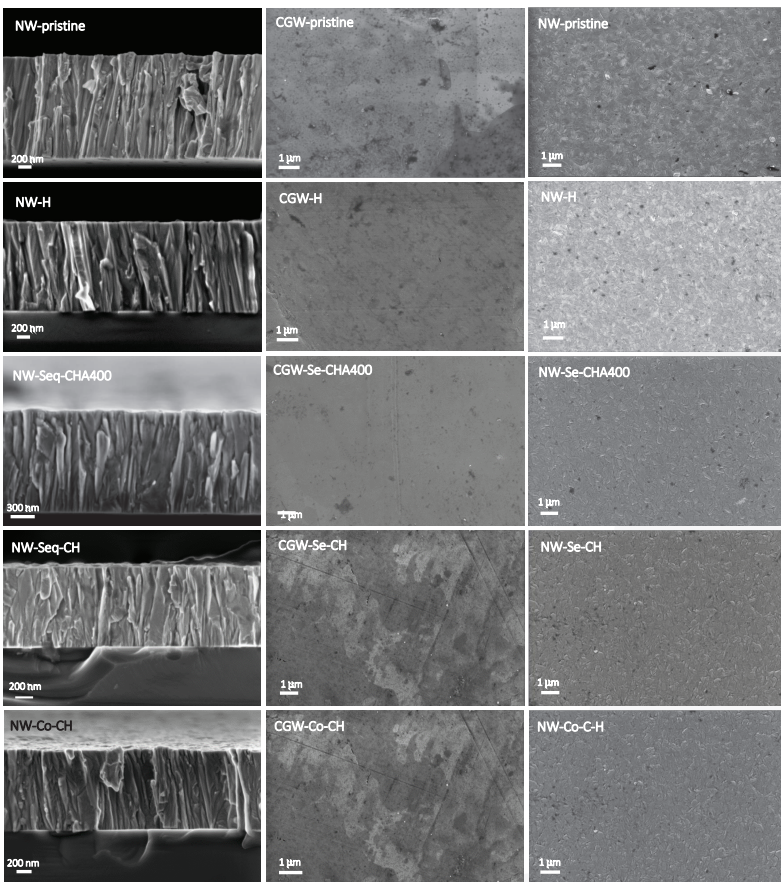
**THE POTENTIAL OF NANOSTRUCTURED W AS PFM IS BEING INVESTIGATED.**

## Objectives

- Study the **stability of the nanostructures** under implantation.
- **Characterization of blistering** if happen in CGW and NW.
- Compare the **microstructure** of the samples **prior to and after implantation**:
- Study the **hydrogen depth distribution** in W as a function of:
  - Sample microstructure  $\Rightarrow$  NW / CGW
  - Implantation conditions:
    - Single implantation / Double implantation.
    - Sequential implantation / Co-implantation.
    - Implantation temperature.

## Morphology of the samples

- Shape and average size of **nanocolumns** are **preserved** after implantation.
- **No blistering** either in CGW or in NW after implantation

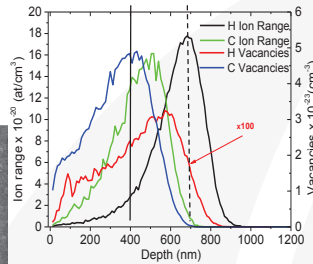


## Conclusions

- Nanostructures are stable under the studied implantations conditions.
- Phase composition of all the samples is preserved after implantation
- H behaviour in NW is dominated by its large density of defects (i.e. grain boundaries).
- H retention is larger in NW than in CGW.
- Synergistic effects have a large influence on H retention in CGW samples but do not in NW samples.
- None of the studied samples present H retention when the hydrogen implantation is carried out at 400°C.
- NW shows a promising behaviour in radiation environments.

## Light species implantation

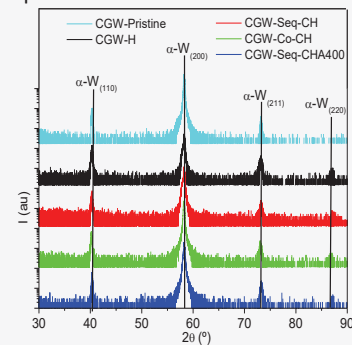
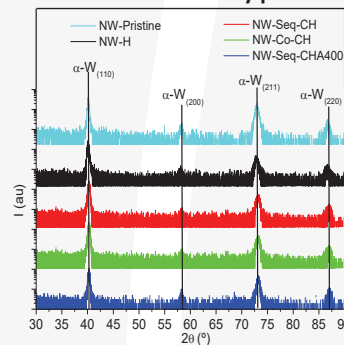
- NW and CGW samples were implanted with **different conditions**:
  - **Single implantation** of H at 170 keV and Room Temperature (RT)
  - **Sequential implantation** of C (665 keV) and H (170 keV):
    - At Room Temperature (RT).
    - At 400 °C.
  - **Co-implantation** of C (665 keV) and H (170 keV).
- Implantations performed at the **Helmholtz-Zentrum Dresden-Rossendorf**.
- Implantation dose was selected to be **5x10<sup>16</sup> cm<sup>-2</sup>**.



SAMPLE CODE	STRUCTURE	H implantation		C sequentially implanted		C co-implanted	
		✓/✗	T (°C)	✓/✗	T (°C)	✓/✗	T (°C)
NW-H	Nano	✓	RT				
CGW-H	Coarse grained	✓	RT				
NW-Seq-CH	Nano	✓	RT	✓	RT		
CGW-Seq-CH	Coarse grained	✓	RT	✓	RT		
NW-Co-CH	Nano	✓	RT			✓	RT
CGW-Co-CH	Coarse grained	✓	RT			✓	RT
NW-Seq-CHA400	Nano	✓	400	✓	RT		
CGW-Seq-CHA400	Coarse grained	✓	400	✓	RT		

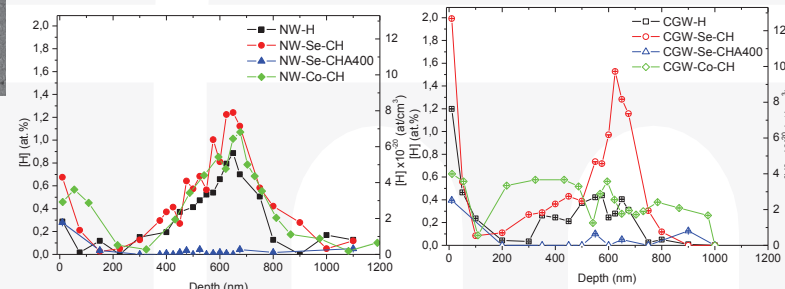
## Microstructure of the samples

- All the studied samples are **polycrystalline and mono-phase** (stable bcc  $\alpha$ -W phase).
- **Absence of secondary phases** upon implantation.



## Hydrogen depth distribution

- H depth distribution was measured at the **Helmholtz-Zentrum Dresden-Rossendorf (HZDR)**.
- Hydrogen depth profiles were obtained by **Resonance Nuclear Reaction Analysis (RNRA)** using the  $H^1(N15, \alpha \gamma)C^{12}$ .



## References

- [1] R. Gonzalez-Arrabal et al. / Journal of Nuclear Materials 453 (2014) 287–295
- [2] N. Gordillo et al. / Applied Surface Science 316 (2014) 1–8
- [3] P.M. Piaggi et al. / Journal of Nuclear Materials 458 (2015) 233–239

# Neutron detectors of $^{10}\text{B}+\text{ZnS}(\text{Ag})$ as an alternative to $^3\text{He}$ -based installed in the Radiation Portal Monitors in homeland Security

<sup>a</sup> K.A. Guzmán, <sup>a</sup> E. Gallego, <sup>b</sup> H.R. Vega-Carrillo, <sup>a</sup> A. Lorente, <sup>c</sup> J.A. González

<sup>a</sup> Departamento de Ingeniería Energética, ETSI Industriales, UPM

<sup>b</sup> Unidad Académica de Estudios Nucleares, Universidad Autónoma de Zacatecas, México

<sup>c</sup> Laboratorio de Ingeniería Nuclear, ETSI Caminos, Canales y Puertos, UPM



## Abstract

Radiation Portal Monitors, RPM, installed in border areas to fight illicit traffic, have the capability of detecting both gamma rays and neutrons. Usually the employed neutron detectors are pressurized  $^3\text{He}$  based neutron detectors tubes, but this is being affected by the scarcity in  $^3\text{He}$  supplies [1]. The aim of this work is to study the suitability of a scintillator detector of  $\text{ZnS}(\text{Ag})$  with a mixture of highly enriched of  $^{10}\text{B}$  [ $^{10}\text{B}+\text{ZnS}(\text{Ag})$ ] as an innovative neutron detectors as replacement to  $^3\text{He}$  detectors. Using MCNPX code, different detectors were studied and their response was calculated for different geometries. The response was estimated through the amount of  $^{10}\text{B}(n,\alpha)^7\text{Li}$  reactions for 29 monoenergetic neutron source, and the reactions induced by a  $^{252}\text{Cf}$  neutron source. Measurements and models were made and we conclude that  $^{10}\text{B}+\text{ZnS}(\text{Ag})$  detectors could be considered as an alternative to the  $^3\text{He}$  detectors. Eventually, a detector is proposed with an optimized geometry able to detect around 2.5 cps-ng of  $^{252}\text{Cf}$ , as recommended by the ANSI Standard [2, 3].

## Materials and Methods

The  $^{10}\text{B}+\text{ZnS}(\text{Ag})$  detectors manufactured by BridgePort Instruments, LLC [4] were tested by the Universidad Politécnica de Madrid (UPM), these detectors are typically cylindrical with only one sensitive layer, or in sandwich-like detectors as the N-48 and N-15 models (Fig. 1) with 5 sensitive layers (Fig. 2). The layers are deposited on plates of PMMA acting as light guide and moderator, surrounded by  $\sim 8\mu\text{m}$  thick aluminum mylar as light reflector. Each detector has a moderator of High Density Polyethylene (HDPE).

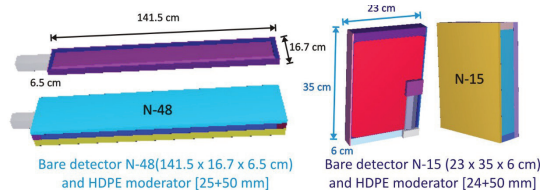


Figure 1. Neutron detectors  $^{10}\text{B}+\text{ZnS}(\text{Ag})$

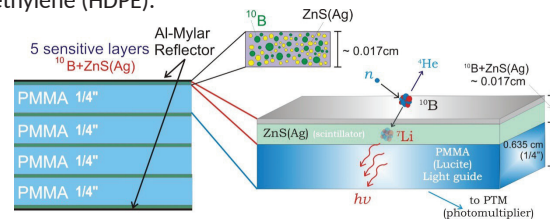
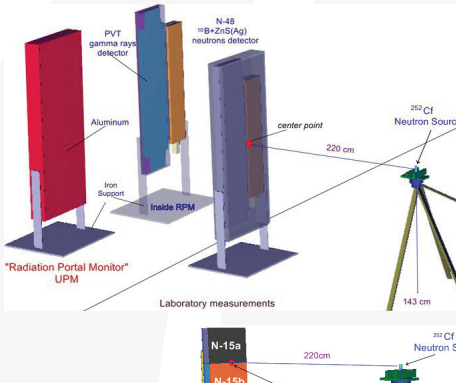
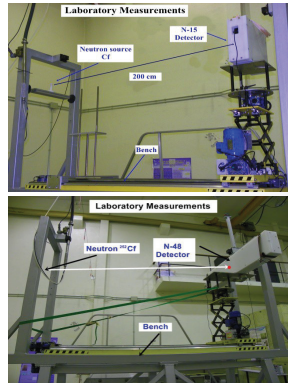
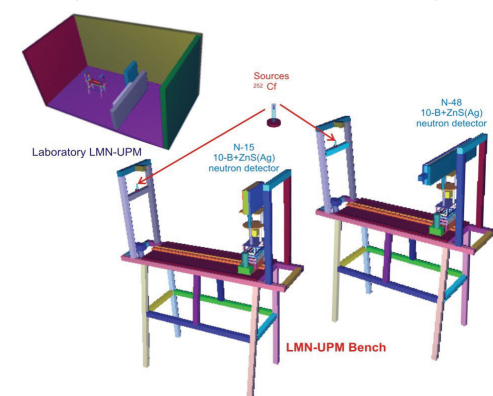


Figure 2. Internal structure of N-48 and N-15 detectors

## Monte Carlo Calculations (MCNPX)

- Sample statistics was large enough to obtain uncertainties less than 3%.
- The cross sections were obtained from the END/B-VI library, also the  $S(\alpha, \beta)$  treatment was included [5].



- Response MCNPX model (N-15 and N-48) to determine the response  $^{10}\text{B}(n,\alpha)^7\text{Li}$  for 29 monoenergetic source  $10^{-9}$  to 20 MeV
- Laboratory [6] MCNPX model (N-15 and N-48) to determine the efficiency for a  $^{252}\text{Cf}$  neutron source as the ANSI Standard [2, 3]
- Outdoor MCNPX model (N-15) to determine the efficiency for a  $^{252}\text{Cf}$  in real operating conditions
- RPM MCNPX model to determine the efficiency for a  $^{252}\text{Cf}$  in a complete Radiation Portal Monitor N-48 with a PVT detector

## Results

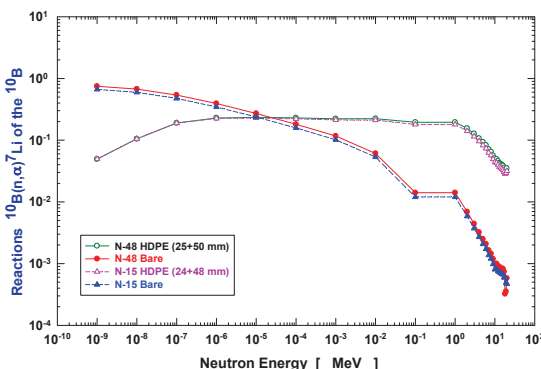


Figure 3. N-15 and N-48 [Bare and with moderator HDPE] Response,  $^{10}\text{B}(n,\alpha)^7\text{Li}$  reactions (per neutron emitted from the sources)

\*  $1\text{ng } ^{252}\text{Cf} \leftrightarrow 2340\text{ n/s}$

Table 1	Indoors	
Detector	Measurements [cps-ng $^{252}\text{Cf}$ ]	MCNPX [cps-ng $^{252}\text{Cf}$ ]
N-48	$1.77 \pm 0.10$	$1.76 \pm 0.01$
N-15	$0.76 \pm 0.20$	$0.73 \pm 0.01$
Outdoor		
N-15	$0.61 \pm$	$0.68 \pm 0.02$
RPM in Laboratory (Indoors)		
N-48	$1.88 \pm 0.20$	$1.91 \pm 0.06$

## Conclusions

The  $^{10}\text{B}+\text{ZnS}(\text{Ag})$  detectors are an interesting alternative to replace  $^3\text{He}$  detectors in RPMs. The N-15 detector is considered suitable for portable backpack systems. The N-48 detector is close to be considered a replacement for  $^3\text{He}$  detectors in RPM. An improvement in the geometry of the detector raising the amount of  $^{10}\text{B}$  increases the detector efficiency aiming to reach 2.5 cps/ng  $^{252}\text{Cf}$ , defined in the ANSI standards a goal to use this type of detectors as an alternative in RPMs [2].

## References

- [1]- R. T. Kouzes, E. R. Siciliano, H. J. Ely, P. E. Keller, R. J. McConn, Nucl. Instrum. Meth. Phys. Res. A, **584**, 383 (2008).
- [2]- ANSI.45.32. American National Standard for Evaluation and Performance of Radiation Detection Portal Monitors for Use in Homeland Security. IEEE National Committee on Radiation Instrumentation, N42. (2006)
- [3]- M. L. Wooldring, J. H. Ely, R. T. Kouzes, D. C. Stromswold, Report PNNL-19726 Pacific Northwest National Laboratory, USA. (2010).
- [4]-BridgePort Instruments, LLC, (2012).
- [5]- H. R. Vega-Carrillo, K. A. Guzmán-García, E. Gallego, A. Lorente, Radiat. Meas., **69**, 30 (2014).
- [6]- H. R. Vega-Carrillo, E. Gallego, A. Lorente, I. P. Rubio, R. Mendez, Appl. Radiat. Isot., **70**, 1603 (2012).



<sup>a</sup> M. Cotelo, <sup>a</sup> E. Oliva, <sup>a</sup> A. González y <sup>a</sup> P. Velarde

<sup>a</sup> Instituto de Fusión Nuclear  
Escuela Técnica Superior de Ingenieros Industriales, UPM  
email: manuel.cotelo@upm.es

## Abstract

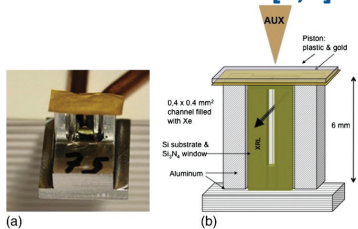
The High Energy Density Physics studies systems with pressures above 1 Mbar (millions of atmospheres) [1]. At this regime ordinary solid matter become compressible and the material will definitely be a ionized medium, a plasma [2]. Such conditions can be achieved in nowadays high-power laser facilities like PALS (Prague Asterix Laser System), OMEGA (Rochester, US) or National Ignition Facility (Livermore, US). In this facilities we can produce strong shock waves (over 10 km/s) that converts ordinary matter into High-Energy-Density matter [3].

Our contribution to the High Energy Density Matter research (which includes several fields like Warm Dense Matter, X-ray lasers or Laboratory Astrophysics) consists in the development of a multiphysics simulation code for laser-created plasmas. This kind of simulations plays a fundamental role in this research area for two reasons: the experimental setup can be improved and optimized and simulations can help us to explain the physical phenomena observed. In this work we present the application of the plasma simulation code to three fields where High Energy Density systems appears.

## 1. Laboratory Astrophysics

One can reproduce astrophysical phenomena at a reduced scale in the laboratory using some physical scaling laws. The laser irradiation will produce a strong shock wave that will bring matter to High Energy Density conditions. That compressed states are equivalent to the states that one can find in astrophysical objects.

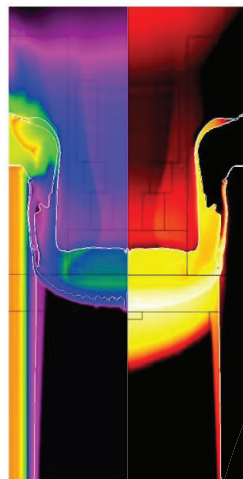
### 1.1 Radiative Shocks [4,5]



The laser (AUX) illuminates a plastic foil and creates a shock wave going down. This shock then goes through a tube filled with Xe.

Radiation produced by the shocked Xe preheats the gas ahead of the shock wave.

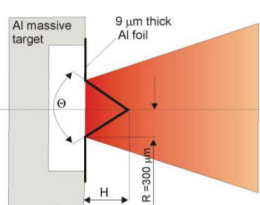
The coupling between hydrodynamics and radiation transport is essential to reproduce the radiative shock.



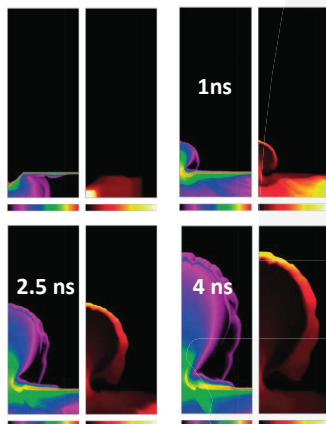
Right: temperatura, eV  
Left: density, kg/m³

### 1.2 Plasma jets [6]

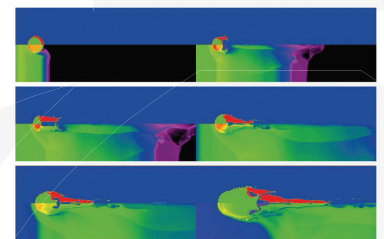
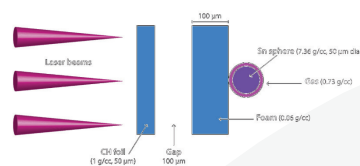
Production of plasma flows at very high Mach number



Left: density, kg/m³  
Right: temperatura, eV



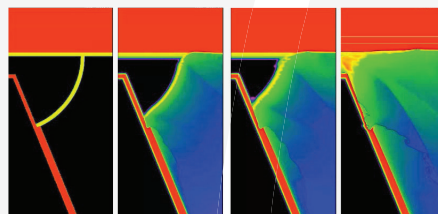
### 1.3 Supernovae remnants



Study of the interaction of a supernovae remnant with the companion star in a stellar binary system. The material ejected by the supernovae reaches the companion star and tear off part of the star atmosphere.

## 2. Inertial Confinement Fusion

### 2.1 Fast Ignition

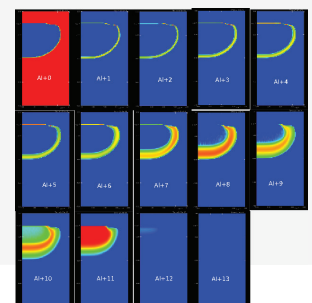
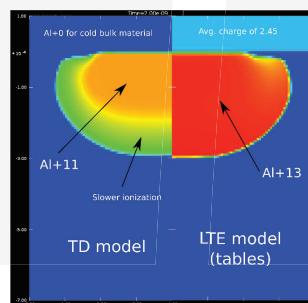


A laser illuminates a plastic semi-sphere with a gold cone inserted.

The capsule is compressed to several times the initial density to achieve the fusion conditions.

## 3. X-ray secondary sources

### 3.1 Laser-created plasmas



Time-dependent atomic physics: this models can obtain the properties of a plasma out of equilibrium. This can occur when a plasma is heated up very quickly with an ultrafast laser pulse.

## References:

- [1] "Frontiers in High-Energy-Density Physics: the X-games of Contemporary Science", National Research Council, The National Academies Press 2003.
- [2] "High-Energy-Density Physics: Fundamentals, Inertial Fusion, and Experimental Astrophysics", R. P. Drake, Springer 2006
- [3] "High Power Laser-matter Interaction", P. Musler, D. Bauer, Springer 2010
- [4] "New probing techniques of radiative shocks", C. Stehlé et al. Optics Communications 285, 1
- [5] "Simulation of radiative shock waves in Xe of last PALS experiments", M. Cotelo et al. High Energy Density Physics (2014)
- [6] "Desarrollo de un método numérico para flujos multimaterial en 2D en ARWEN", D. Portillo, Tesis Doctoral.

## Abstract

Seeding High Order Harmonics in plasma amplifiers holds the promise of table-top, ultra-intense and coherent soft X-ray beams ( $\lambda = 1 \text{ nm} - 40 \text{ nm}$ ). This source would complement and, in some cases, improve the capabilities of current fourth generation light sources. The amplification of HOH in plasma amplifiers created from gas targets, Zeitoun *et al. Nature* (2004) and solid targets, Wang *et al. Nature Photonics* (2008) has been demonstrated and characterized. However, the energy obtained was of the order of hundreds of nanoJoules and the shortest duration achieved was 1 ps. In order to build an useful source, it is needed a thorough theoretical and experimental optimization work. These sources have potential applications in such different fields as industry (defect-free lithography), environment and defence (remote detection of atmospheric contaminants), materials science and biology (single shot imaging) and medicine (low dose tomography).

## 1. DeepOne, a 1D Maxwell-Bloch model

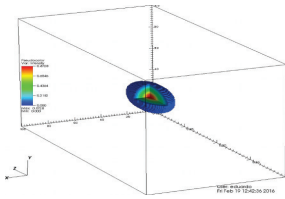
The temporal evolution of seeded HOH along the plasma is modelled using our 1D time-dependent Maxwell-Bloch code DeepOne, Oliva *et al. Phys. Rev. A* (2011)

$$\frac{\partial E}{\partial z} = \frac{i\omega_0}{2c} \left[ \mu_0 c^2 P - \left( \frac{\omega_p}{\omega_0} \right)^2 E \right]$$

$$\frac{\partial P}{\partial \tau} = \Gamma - \gamma P - \frac{iz_{21}^2}{\hbar} E (N_2 - N_1)$$

$$\frac{\partial N_{1,2}}{\partial \tau} = \sum_k C_{k-1,2} N_k \pm \Im(E^* P) \frac{1}{2\hbar}$$

A 3D time-dependent Maxwell-Bloch code, Dagon<sup>\*</sup> is under development under the framework of the FP7 Marie Skłodowska-Curie IEF project DAGON.



## 2. Towards ultraintense soft X-rays

Hot, dense plasmas release the energy stored in time, i.e. the population inversion is continuously recovered by electron collisional excitation. Thus, increasing the temporal duration of the seed before amplification and recompressing it afterwards (i.e. a transposition of the Chirped Pulse Amplification technique) allows to extract a maximum of energy while maintaining the short duration of the pulse, Oliva *et al. Nature Photonics and Optics Letters* (2012).

**LETTERS**  
PUBLISHED ONLINE: 21 OCTOBER 2012 | DOI: 10.1038/NPHOTON.2012.240

**A proposal for multi-tens of GW fully coherent femtosecond soft X-ray lasers**

E. Oliva<sup>1</sup>, M. Fajardo<sup>2</sup>, L. Li<sup>1</sup>, M. Pittman<sup>1</sup>, T. T. T. Le<sup>1</sup>, J. Gautier<sup>1</sup>, G. Lambert<sup>1</sup>, P. Velarde<sup>1</sup>, D. Ros<sup>1</sup>, S. Sebban<sup>1</sup> and Ph. Zeitoun<sup>1\*</sup>

## 3. Measuring the gain recovery time

The gain recovery time was measured by seeding two HOH with a variable delay and measuring their relative amplification. The agreement between experiment and model is excellent, showing that HOH is a very convenient tool to probe atomic processes in hot, dense plasmas, Wang *et al. Nature Photonics* (2014).

**LETTERS**  
PUBLISHED ONLINE: 20 APRIL 2014 | DOI: 10.1038/NPHOTON.2014.76

**Gain dynamics in a soft-X-ray laser amplifier perturbed by a strong injected X-ray field**

Y. Wang<sup>1</sup>, S. Wang<sup>1</sup>, E. Oliva<sup>2</sup>, L. Li<sup>1</sup>, M. Bernillo<sup>1</sup>, L. Yin<sup>1</sup>, J. Nejdli<sup>1</sup>, B. M. Luther<sup>1</sup>, C. Proux<sup>1</sup>, T. T. T. Le<sup>1</sup>, J. Duvvuri<sup>1</sup>, D. Ros<sup>1</sup>, Ph. Zeitoun<sup>1\*</sup> and J. J. Rocca<sup>1\*</sup>

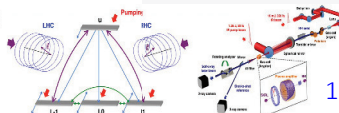
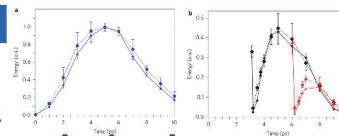
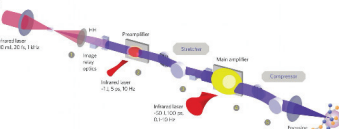
## 4. Amplifying circularly polarized HOH

Many applications require circularly polarized HOH, ideally with enough energy to do single-shot images. It has been demonstrated experimentally that circularly polarized HOH conserve its polarization state when passing through a plasma amplifier. Our model confirms this result, Depresseux *et al. Phys. Rev. Lett.* (2015).

**PHYSICAL REVIEW LETTERS**  
PUBLISHED ONLINE: 21 AUGUST 2015 | DOI: 10.1103/PhysRevLett.115.083901

**Demonstration of a Circularly Polarized Plasma-Based Soft-X-Ray Laser**

A. Depresseux<sup>1</sup>, E. Oliva<sup>2</sup>, J. Gautier<sup>1</sup>, F. Tissandier<sup>1</sup>, G. Lambert<sup>1</sup>, B. Védughe<sup>1</sup>, J.-P. Godke<sup>1</sup>, A. Tafa<sup>1</sup>, J. Nejdli<sup>1</sup>, M. Kozlova<sup>1</sup>, G. Maynard<sup>1</sup>, H. T. Kim<sup>1</sup>, K. Ta Phuoc<sup>1</sup>, A. Rousse<sup>1</sup>, P. Zeitoun<sup>1</sup> and S. Sebban<sup>1</sup>



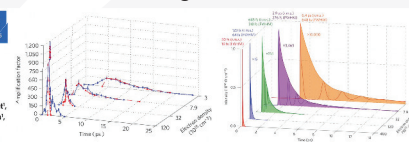
## 5. Ultra-short soft X-ray beams

Modelling suggests that increasing the electron density will result in shorter pulses (via collisional broadening and ionization). Tens of femtosecond pulses have been achieved seeding a Kr<sup>8+</sup> amplifier with  $n_e = 1.2 \times 10^{20} \text{ cm}^{-3}$ . The model reproduces the experimental results along a wide range of densities (more than two orders of magnitude), Depresseux *et al. Nature Photonics* (2015). Pulses shorter than 20 fs are envisaged.

**LETTERS**  
PUBLISHED ONLINE: 15 NOVEMBER 2015 | DOI: 10.1038/NPHOTON.2015.225

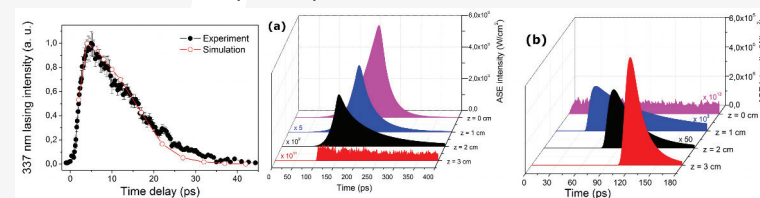
**Table-top femtosecond soft X-ray laser by collisional ionization gating**

A. Depresseux<sup>1</sup>, E. Oliva<sup>2</sup>, J. Gautier<sup>1</sup>, F. Tissandier<sup>1</sup>, J. Nejdli<sup>1</sup>, M. Kozlova<sup>1</sup>, G. Maynard<sup>1</sup>, J. P. Godke<sup>1</sup>, A. Tafa<sup>1</sup>, A. Ufchitz<sup>1</sup>, H. T. Kim<sup>1</sup>, S. Jacquemont<sup>1</sup>, V. Malka<sup>1</sup>, K. Ta Phuoc<sup>1</sup>, C. Thauy<sup>1</sup>, P. Rousseau<sup>1</sup>, G. Iaquaniello<sup>1</sup>, T. Lefrou<sup>1</sup>, A. Flacco<sup>1</sup>, B. Védughe<sup>1</sup>, G. Lambert<sup>1</sup>, A. Rousse<sup>1</sup>, P. Zeitoun<sup>1</sup> and S. Sebban<sup>1\*</sup>



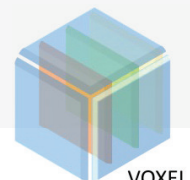
## 6. Remotely induced atmospheric Nitrogen lasing

Backward lasing of neutral Nitrogen molecules  $\text{C}^3\Pi_u \rightarrow \text{B}^3\Pi_g$  has important applications in remote atmospheric sensing. Our Maxwell-Bloch model reproduces quite well experimental results, providing a deeper insight in the atomic physics of atmospheric plasmas and the characterization of the backwards-emitted amplified spontaneous emission.



## 7. Low dose X-ray tomography

Computerized Tomography (CT) has been one of the greatest achievements in medical imaging, but at the cost of a high, potentially harmful, X-ray irradiation dose. VOXEL, a H2020-FETOPEN-2014-2015-RIA project aims to provide an alternative to tomography with a disruptive technology enabling 3D X-ray imaging at very low dose. The underlying technology, a Light Field Camera (LFC), is a form of wavefront sensor, recording not only the 2D image but also the direction of the incoming rays.



## 8. Collaborations



## Acknowledgements

The authors would like to thank the financial support provided by the Spanish MINECO within the program No. ENE2012-32108, LASERLAB II 228334 SFINX European Project, RTRA Triangle de la Physique project SHYLAX, Agence Nationale de la Recherche Project No. ROLEX ANR-06-BLAN-04 023 01, COST Action MP1203, the Marie Skłodowska-Curie FP7-PEOPLE-2013-IEF 627191 DAGON and the H2020-FETOPEN 665207 VOXEL. <http://www.goominet.com/unspeakable-vault-of-doom/faq/>





## Seismic Engineering

- [SEI - 01] 203 *"Active crustal deformation of the El Salvador Fault Zone (ESFZ) using geodetic data: Implications in seismic hazard assessment."* Staller, Alejandra; Benito, Belén; Gaspar-Escribano, Jorge; Martínez-Cuevas, Sandra; Torres, Yolanda; Ruiz-Barajas, Sandra; Quirós, Ligia Elena; Yazdi, Pouye.
- [SEI - 02] 204 *"Does the Spatial Analysis of 2012 Ahar-Varzeghan Seismic Sequence Corroborate the Tectonic Interpretations?"* Yazdi, Pouye; Gaspar-Escribano, Jorge; Staller, Alejandra; Benito, María Belén; Martínez-Cuevas, Sandra; Torres, Yolanda; Ruiz Barajas, Sandra; Quirós, Ligia Elena.
- [SEI - 03] 205 *"Remote Sensing and Earthquake Engineering: seismic vulnerability assessment based on LiDAR, ortho-photo and satellite image analysis."* Torres, Yolanda; Martinez-Cuevas, S.; Haghi, A.; Quirós, Ligia Elena; Gaspar-Escribano, Jorge; Benito, B.; Staller, Alejandra; Ruiz-Barajas, Sandra; Yazdi, Pouye.
- [SEI - 04] 206 *"Seismic behavior of reinforced concrete waffle-flat plate structures with hysteretic dampers."* Galé, David; Benavent, Amadeo.
- [SEI - 05] 207 *"Seismic upgrading of frame structures with a soft first story by using hysteretic dampers."* Mota, Santiago Félix; Climent, Amadeo Benavent.
- [SEI - 06] 208 *"Seismic vulnerability assessment incorporating urban parameters that influences buiding damage."* Martínez-Cuevas, Sandra; Torres, Yolanda; Gaspar-Escribano, Jorge; Benito, María Belén; Staller, Alejandra; Quirós, Ligia Elena; Ruiz-Barajas, Sandra; Yazdi, Pouye.
- [SEI - 07] 209 *"Development of new energy dissipators for the passive control in structures subjected to earthquakes."* Benavent, Amadeo; Mota, Santiago Félix; Villafañá, Oscar; Galé, David.
- [SEI - 08] 210 *"How new fault data and models affect seismic hazard results? Examples from southeast Spain."* Gaspar-Escribano, Jorge; Benito, María Belén; Staller, Alejandra; Ruiz Barajas, Sandra; Quirós, Ligia Elena; Yazdi, Pouye; Martínez-Cuevas, Sandra; Torres, Yolanda.
- [SEI - 09] 211 *"Seismic Hazard map of Spain for the revision of the Spanish Building Code."* Benito, Belén; Ribas, Alicia; Gaspar-Escribano, Jorge; Staller,



Alejandra; Ruiz Barajas, Sandra; Quirós, Ligia Elena; Yazdi, Pouye; Martínez-Cuevas, Sandra; Torres, Yolanda.

# Active crustal deformation of the El Salvador Fault Zone (ESFZ) using geodetic data: Implications in seismic hazard assessment

<sup>a</sup>Alejandra Staller, Belén Benito, Jorge Gaspar Escribano, Sandra Martínez-Cuevas, Yolanda Torres, Sandra Ruiz-Barajas, Ligia-Elena Quirós, Pouye Yazdi

<sup>a</sup>Departamento de Ingeniería Topográfica y Cartografía. ETSI Topografía, Geodesia y Cartografía. Universidad Politécnica de Madrid (a.staller@upm.es)

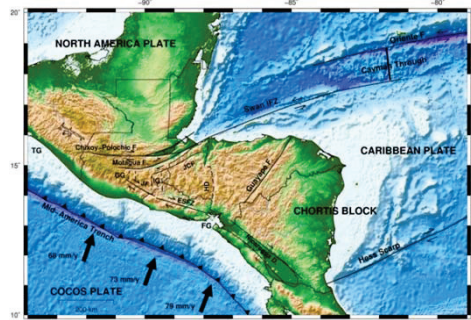


## Abstract

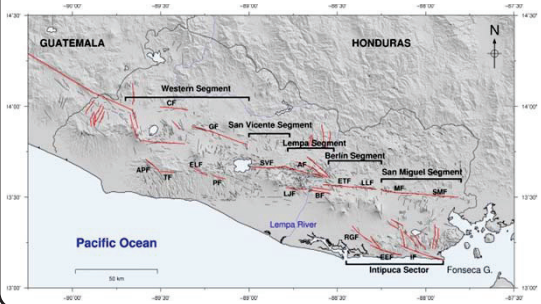
The current work aims at understanding active crustal deformation of the El Salvador Fault Zone through kinematic model. The results provide significant information to be included in a new estimation of seismic hazard taking into account the major structures in ESFZ.

## I. SEISMOTECTONIC SETTING

El Salvador Fault Zone (ESFZ) is a deformation band that extends across the whole country within the Salvadorian volcanic arc (Martínez-Díaz et al., 2004) and is responsible for frequent earthquakes, some of high magnitude, as the February 13, 2001 earthquake with Mw 6.6. The ESFZ continues westward and is relieved by the Jalpatagua Fault in Guatemala. Eastward ESFZ becomes less clear disappearing at Fonseca Gulf.



The ESFZ deforms and offset quaternary deposits with a right lateral movement in its main segments (Corti et al., 2005). Five segments have been proposed for the whole fault zone, from the Jalpatagua Fault to the Fonseca Gulf (Canora et al., 2010).



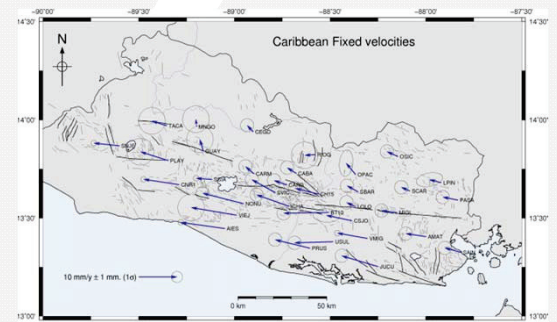
## II. GPS VELOCITY FIELD

### GPS DATA

In 2007 we established 23 new GPS campaign stations that together with previous 7 stations (Alvarado et al, 2011) forming the ZFESNet (Staller et al., 2016). The main aim of the ZFESNet is quantify the current interseismic deformation associated with ESFZ. We have carried out 4 GPS campaigns of the ZFESNet from 2007 to 2012. The processing of the registered observations was done using the Bernese 5.0 software (Dach et al., 2007).

### INTERSEISMIC VELOCITY FIELD

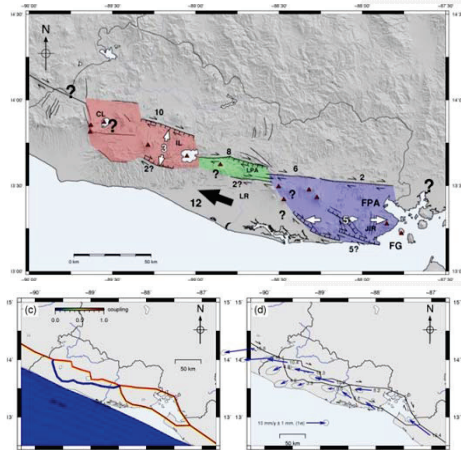
We have estimated velocities and their uncertainties for each station referred to ITRF2008 and Caribbean plate fixed. The interseismic velocity field shows a typical deformation pattern of a strike-slip fault fully coupled, with dextral strike-slip tectonics along the ESFZ.



## III. MODELING OF CRUSTAL DEFORMATION

We used a three-dimensional elastic dislocation model by integrating geodetic (GPS), geological and seismological data (McCaffrey, 2002)

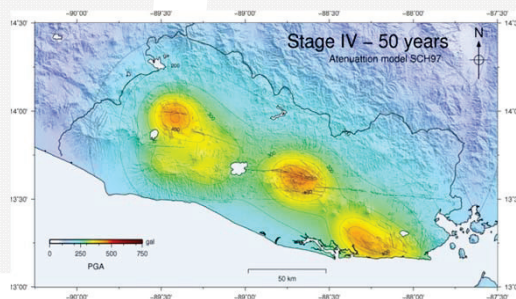
Modeling results reject the existence of a simple structure with a single slip zone along the volcanic arc in El Salvador, suggesting the necessity to introduce two intermediate blocks between the Caribbean and forearc main blocks.



Additionally, the Salvadoran volcanic arc faults are almost totally blocked. Finally, modeling results confirm that the degree of coupling at the interface of the subduction zone off the Salvadoran coast is practically null.

## IV. IMPLICATIONS IN SEISMIC HAZARD

The results obtained help refining the definition and characterization of seismogenic sources used for the seismic hazard assessment of El Salvador, allowing the introduction of some faults as independent for hazard calculations.



Different seismic hazard maps are computed considering only fault sources, predicting maximum Peak Ground Acceleration (PGA) values of 0,6 g in the vicinity of some faults.

## V. CONCLUSIONS

We have presented the preliminary results, conclusions and implications obtained based on the GPS data compiled over this 5-year period, which have been essential to understanding and learning about the kinematics in this area.

The deformation field obtained from the original data, the estimates of locking depth, strike-slip rates and degree of coupling and the recurrence periods obtained for characteristic earthquakes are all important and essential steps towards learning about this fault system and seismic hazard in El Salvador.

Results suggest that the boundary between the Salvadoran forearc and Caribbean blocks is a deformation zone that varies from west to east along the ESFZ. A long-term velocity of the Salvadoran forearc of  $13,5 \pm 1$  mm/a with ~NO direction is estimated considering the Caribbean plate as the reference frame.

The strain distribution along the ESFZ confirms the transfer of deformation from the western segments of ESFZ to extensional structures distributed over a large area on the eastern end of the fault zone.

The results obtained improve estimates of seismic hazard in El Salvador by introducing modeled faults as independently estimated seismogenic sources.



## Abstract

On 11 August 2012, two destructive shallow earthquakes  $M_w=6.4$  and  $M_w=6.2$  occurred within distance of about 6 km and time lag of 11 minutes in Northwestern Iran between the small cities of Ahar and Varzeghan with no previously well known active fault or significant seismicity. The following aftershock sequence remained strongly active during four months with more than 3500 events registered by the Iranian Seismological Center in an area within a radius of 50 km. The magnitude distribution of the sequence gives a b-value of 0.97 for cutoff magnitude  $M_w=2.0$ .

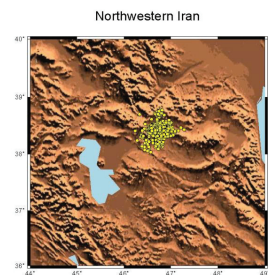


**Figure 1)** Location of the sequence in Northwestern Iran

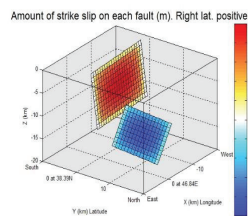


**Figure 2)** Relative location of the fault rupture geometries considered in this study, including a smoothed elliptical source model for the slip on the fault.

	1st Shock $M_w=6.4$	2nd Shock $M_w=6.2$
Strike, Dip, Rake (source)	267, 81, -175 (IRSC)	7, 51, 21 (IRSC)
Depth to Top	0 km	11 km
Epi (lat, long)	38.39 N, 46.84 E	38.42 N, 46.77 E
Hypo Depth	6 km	13 km
Fault Size	22 x 12 km	15 x 9 km

## 2) CFS Changes Due To The First Mainshock

The coulomb stress change because of the first mainshock was studied in order to see if it has triggered the second mainshock. Considering the epicenter given by Donner et al. 2015 and with the mentioned geometry for the first mainshock, it is more likely that the second shock had happened at a hypocentral depth lower than the edge of the first fault. using a smoothed elliptical source model the slip was weighted over the fault plane considering the released energy. A fiction coefficient of 0.4 was considered since the faulting is strike slip.

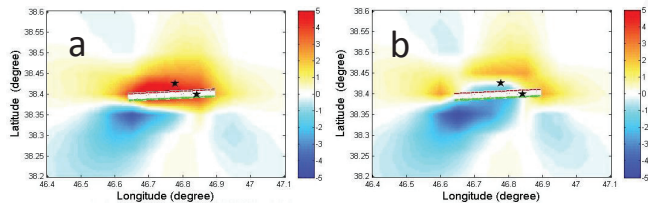


**Figure 5)** CFS (bar) due to the 1st shock with 267-81-(-175) with smoothed elliptical weighting to the slip amount and for the 2nd shock with 7-57-21 on a horizontal plane with a) 12 Km depth and b) 13 Km depth. Slip was calculated using Wells and Coppersmith (1994) empirical relation for average slip and Hanks and Kanamori (1979) relation for released energy.

## 4) Conclusions

Based on our knowledge from previous works investigating the mechanism of the faulting for the doublet of Ahar-Varzeghan, we tried to find the best explanation using the changes in the coulomb failure stress and the aftershock sequence spatial distribution in different depths. The results for the assumption of North-South orientation plane for the second mainshock at lower depth in respect to the first shock's fault, was presented in this study. This assumption made us to be able to justify the spatial distribution of the sequence coming during 4 months and improve our understanding about the source placement. The agreement between the spatial distribution of more than 500 relocated data at the mean depth of 14 km with the CFS changes for the optimum strike slip faulting (as the most probable regional mechanism) leads us to accept that the doublet most likely occurred on a perpendicular structure and corroborate with the result of previous studies.

## 5) References

- A. Copley et al. 2014, "The 2012 August 11 Ahar earthquakes: consequences for tectonics and earthquake hazard in the Turkish-Iranian Plateau", *Geophysics Journal International* 196, 15–21
- S. Donner et al. 2015, "The Ahar-Varzeghan Earthquake Doublet ( $M_w$  6.4 and 6.2) of 11 August 2012: Regional Seismic Moment Tensors and a Seismotectonic Interpretation", *BSSA*, Vol. 105, No. 2a
- M. Faridi et al. 2012, "The Ahar-Varzeghan Earthquake Doublet ( $M_w$  6.4, 6.2, Iran)", *Geological Survey of Iran*
- M. Mahood et al. 2014 "Simulation of the first earthquake August 11, 2012 Ahar-Varzeghan using stochastic finite fault method", *Iranian Journal of Earth and Space Physics*, Vol 40, No.2

An observed surface rupture which starts at 4 km west of the first mainshock continues about 8 km westward. Most probably the rupture was due to the first mainshock mainly because the rupture orientation and focal mechanism of the second shock do not agree.

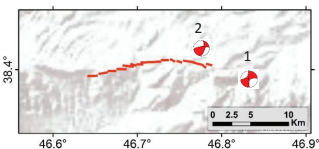


**Figure 3)** Surface rupture location

## 1) Re-localization

The seismicity since August 2012 to the end of November 2012 has been re-localized using double difference algorithm of Waldhauser and Ellsworth (2000).

The maximum distance of 200 km was considered between a pair and station and maximum distance of 15 km for each pair of events. The principal cluster has over 600 events with centroid at  $\sim 38.42N$ ,  $\sim 46.74E$  and  $\sim 13.40$  Km depth. For the velocity model the result of study by Donner et al.(2015) was used. (7 layers and  $V_p/V_s$  ratio 1.7)

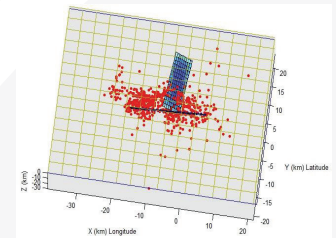


**Figure 4)** Gap between the re-located sequence and the location of the faults

## 3) CFS Changes Due To The Doublet

**Regional stress:** looking at the regional stress map If we consider a mean angle of 135 for maximum horizontal stress in the area on the and assume an approximately zero plunge then the optimum strike slip faulting will be on vertical planes that have angle of  $\delta=(2\beta)'$  with the maximum horizontal stress. It means an angle of 169 for left lateral and 101 for a right lateral planes for  $\mu=0.4$ .

**Coulomb Failure Stress Changes:** For strike, dip and rake of 101,90 and 180 the change of CFS due to both mainshocks and for frictional coefficient 0.4 and 0.6 for the strike slip and strike slip with inverse components respectively were calculated. The main focus was on depths between 11 to 17 km and the result shows high density of the events on the positive stress change areas. The CFS changes for optimum rives and normal planes was also calculated.

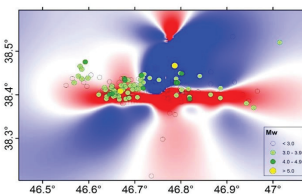


**Figure 6)** CFS changes at a depth of 12 km and events with depth between 11-13 km : 75 % in the positive stress changes area

**Figure 7)** CFS changes at a depth of 14 km and events with depth between 13-15 km : 72 % in the positive stress changes area

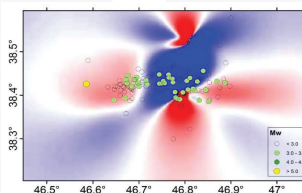


**Figure 8)** CFS changes at a depth of 16 km and events with depth between 15-17 km : 55 % in the positive stress changes area

-5 bar      +5 bar



<sup>a</sup>Y. Torres, <sup>a</sup>S. Martinez-Cuevas, <sup>a</sup>A. Haghi, <sup>a</sup>L.E. Quiros, <sup>a</sup>J. Gaspar-Escribano, <sup>a</sup>B. Benito, <sup>a</sup>A. Staller, <sup>a</sup>S. Ruiz-Barajas, <sup>a</sup>P. Yazdi.

<sup>a</sup>Earthquake Engineering Research Group (y.torres@upm.es)



## Abstract

Seismic risk assessment usually involves the characterization and analysis of an exposed building stock according to vulnerability-relevant attributes and integrates it with the outcomes of a seismic hazard analysis of the same area to compute expected damage distributions. The collection of exposure and vulnerability data frequently turns into a challenging task due to:

- (1) Traditional sources, such as cadaster, is not always available, accessible, updated, or complete
- (2) Field campaigns are time- and resource- consuming.

Hence new techniques for exposure and vulnerability assessment that are able to cope with the high urbanization rate of cities need to be developed. The analysis of remotely sensed data, such as satellite and aerial multi-spectral images or LiDAR points, can provide valuable information about the buildings, to be used in a vulnerability assessment.

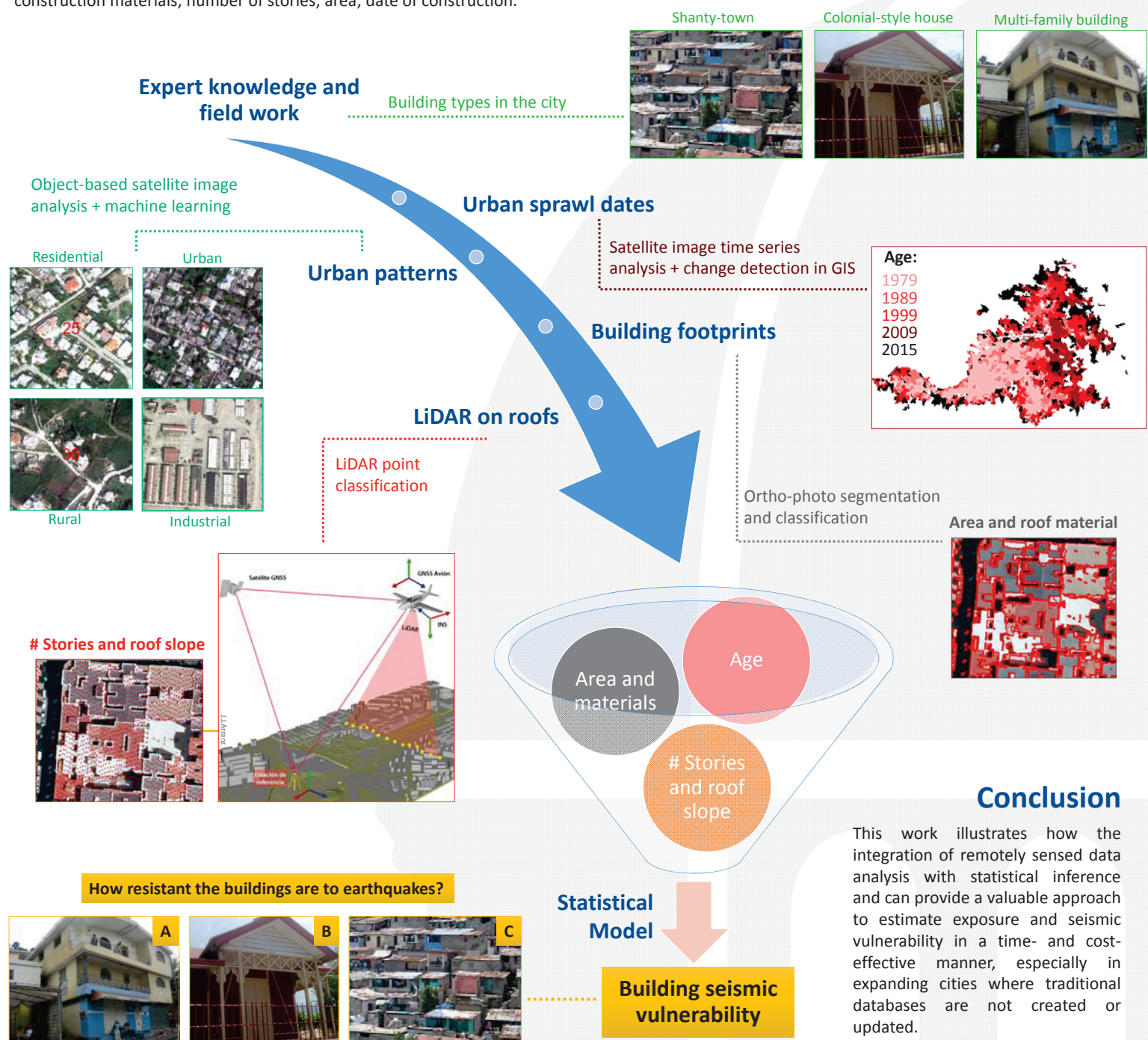
In this poster we present a holistic procedure for exposure and vulnerability estimation, that combines traditional with novel techniques to create an exposure database of the built environment.

## Exposure and vulnerability database

To be usable for vulnerability allocation, the exposure database should have at least the following fields with information about the buildings of a city : construction materials; number of stories; area; date of construction.

## How to create this database?

By following the next procedure:



## Conclusion

This work illustrates how the integration of remotely sensed data analysis with statistical inference can provide a valuable approach to estimate exposure and seismic vulnerability in a time- and cost-effective manner, especially in expanding cities where traditional databases are not created or updated.



<sup>a</sup> David Galé, <sup>a</sup> Amadeo Benavent

<sup>a</sup> Department of Mechanical Engineering, Polytechnic University of Madrid, Spain  
(david.gale@upm.es and amadeo.benavent@upm.es)

## Abstract

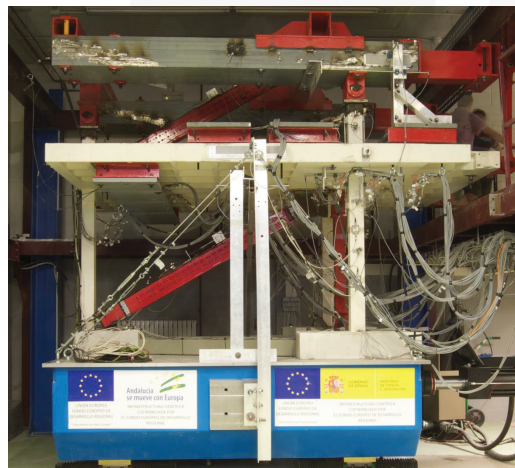
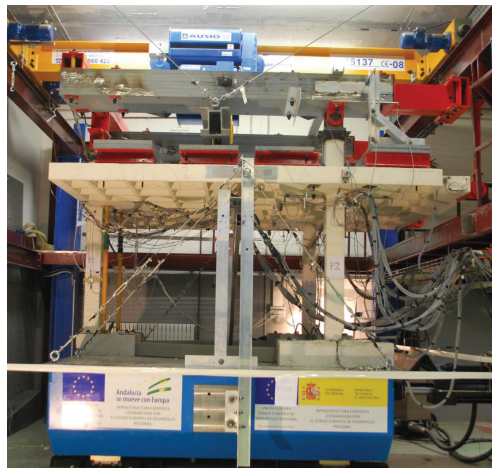
RC waffle-flat plate structures are recognized as having very poor performance when used as main earthquake-resistant system (low ductility, high flexibility and proneness to concentrate damage). However it is one of the most widely used typology due to its ability to sustain gravity loads with large spans. On the other hand, one of the new technologies of passive control consists on using special devices called “energy dissipators” that are able to absorb most of the energy input by the earthquake and prevent damage on the main structure. One of the research lines of the Group is to investigate a new mixed system that combines in parallel two parts: RC waffle-flat plates supported on isolated columns (main structure) and energy dissipators. Past results of this Group show that with this mixed system more efficient and sustainable structures can be achieved.

## Waffle-flat plates systems under seismic hazard

Reinforced concrete (RC) structures consisting of waffle-flat plates (WFP system herein) are very competitive for resisting gravitational loads in comparison with others typologies. Since, its cost in formworks is reduced, they allow more freedom in locating the columns in plan and can accommodate large spans with relatively small plate depths. Nevertheless, WFP systems present two important drawbacks for resisting seismic loads: low horizontal stiffness and limited ductility. To counteract these shortcomings, new technologies of passive control are included in the structure in form of hysteretic dampers, in order to absorb a large portion of the seismic energy. In such away, decoupling the mechanism that bears the gravity loads up from the mechanism that absorbs the lateral seismic loads lead to more efficient and sustainable structures.

## Experimental approach

Several specimens were casted and tested by a shaking table that reproduced real earthquakes. The goal of research was to investigate the dynamic behaviour of WFP system designed with and without dampers under realistic conditions, that is, subjecting material to strain rates and cycles of forced random displacements typical of real earthquakes.



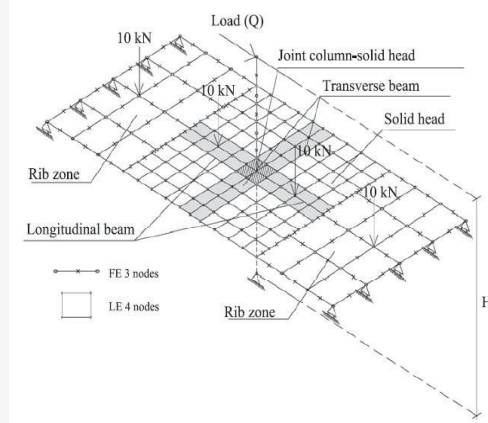
## Outline of the research

Currently, we study the viability and application of “energy dissipators” for RC structures with waffle-flat plates in moderate earthquake-prone regions. We focus on:

- Solutions to accommodate dampers on the structure
- Evaluation of the overall ductility due to the dampers
- Quantification of cost reduction in the main structure due to the use of dampers
- Quantification of improvements on seismic response
- The development of energy-based methods for designing this type of mixed systems.
- Validation of the design method and evaluation of the overall response through numerical simulations and shaking table test.

## Numerical approach

Non lineal numerical FEM models that represented column-WFP connections were developed, calibrated with experimental results. These models served to conduct extensive parametric studies.

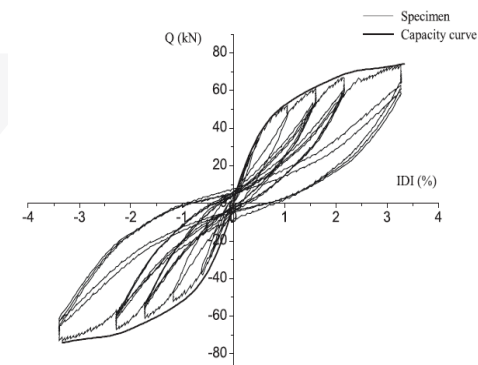


## Past results

- The combination WFP system supported on isolated columns with hysteretic dampers is viable and shows a superior seismic performance than the conventional solution without dampers.
- At least, two possible solutions for the dampers are possible: (a) as diagonal bars; (b) on plate's depth
- An energy-based design method was initially develop to design the dampers
- Numerical simulations and several dynamic tests conducted with a shaking table served to validate the proposed design method and assess the satisfactory seismic performance of the proposed system.

## Future work

Future research is focussed in studying the torsion effects in asymmetric WFP structures with dampers, subjected simultaneously to two horizontal components of ground motion.



## Abstract

The present study focuses on the application of hysteretic dampers to the seismic retrofit of a particular type of existing building: that consisting on reinforced concrete frames with a soft first story. Energy dissipating devices (EDDs) are new technologies capable of minimizing inter-story drifts and increasing the earthquake resistance of buildings. This investigation presents an innovative solution for seismic upgrading this type of structures that consists on combining in the first (ground) story the installation of hysteretic dampers with the reinforcement of beams/columns with advanced composite materials (Fiber Reinforced Polymer laminates *FRP* and Steel Reinforced Polymer spikes *SRP*). The rest of stories, which lateral stiffness and strength is typically high in comparison to the first story due to the presence of infill walls, are not retrofitted. In this study, several numerical models representing existing buildings with 3 and 6 stories were developed. The models were seismic upgraded with the solution proposed by the authors and subjected to several natural accelerograms. The results of the non-linear dynamic response analyses show that the proposed solution is feasible. Finally, a simple method to design the proposed seismic upgrading solution is outlined. The method is based on the theory of energy balance of Housner-Akiyama.

## Introduction and Objective

One of the most common and dangerous seismic deficiencies in existing concrete building is the soft first story, this structural configuration is undesirable and is characterized by the absence of masonry infills walls at the ground floor while they are present at the elevation stories (*figure 1*). Many buildings with soft ground story collapsed in past earthquakes (*Figure 2*), and they are a matter of big concern especially in regions of high seismicity such as Dominican Republic. Few investigations have been carried out in order to propose a solution to existing buildings with soft story configuration. *Figure 3* shows the schematic solution proposed in this work. The main objective of this study is to achieve a structure able to dissipate most of the energy input by the earthquake in the first story, approaching the behavior of the base isolation systems.



**Figure 1:** Typical residential building with soft first story in Dominican Republic

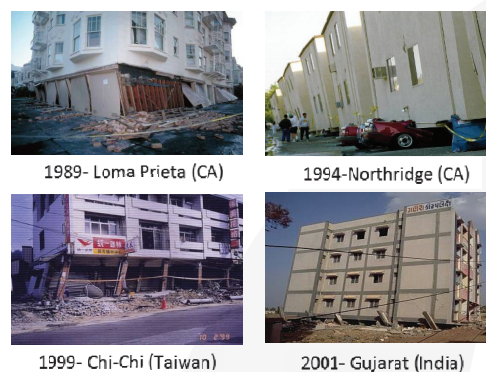


**Figure 2:** Examples of soft first story building collapse

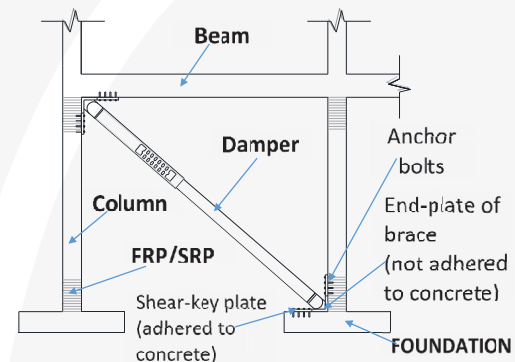


**Figure 3:** Proposed solution schema, hysteretic damper and FRP/SRP

## Methodology

To achieve the main goal, several numerical models representing existing buildings with 3 and 6 stories (*Figure 4*) were developed. Next, a simple method to design the proposed seismic upgrading solution is outlined. The method is based on the theory of energy balance of Housner-Akiyama. Finally, the three models developed were subjected to several natural accelerograms, corresponding to impulsive and non-impulsive earthquakes respectively, and following the performance based seismic design philosophy (PBSD).

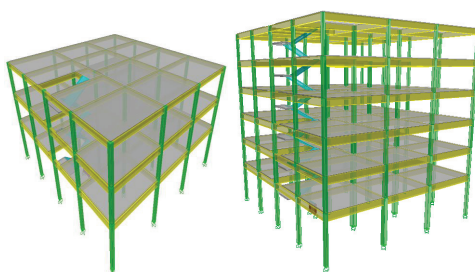


**Figure 4:** Reinforced concrete prototypes

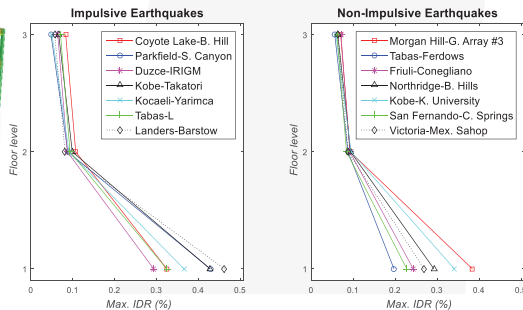


**Figure 5:** Maximum IDR for 3 story prototype

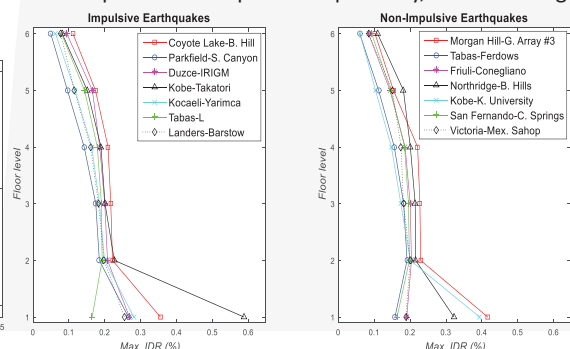


**Figure 6:** Maximum IDR for 6 story prototype

## Results

Figures 5 and 6 show the response of the 3 and 6 story prototypes respectively, in terms of the inter-story drift ratio (IDR). IDR is computed as ratio of the maximum inter-story drift at any story to the corresponding story height. It is important to remark that the results presented here corresponds to buildings without any local modification (i.e. without *FRP/SRP* strengthening) besides installing hysteretic dampers. It can be seen in Figures 5 and 6 that the IDR remain within acceptable limits. Within these limits, the damage in the RC columns is negligible.

## Conclusions

The main conclusion of the present investigation is that the proposed retrofitting solution protects satisfactorily the existing structure and prevents damage under severe earthquakes.

## Future work

Propose optimal combination of different seismic upgrading strategies (traditional and innovative) to mitigate the soft story problem, and conduct shaking table tests.



# SEISMIC VULNERABILITY ASSESSMENT INCORPORATING URBAN PARAMETERS THAT INFLUENCES BUILDING DAMAGE

<sup>a</sup>Sandra Martínez-Cuevas, Yolanda Torres, Jorge M. Gaspar-Escribano, M. Belén Benito, Alejandra Staller, Ligia-Elena Quirós, Sandra Ruiz Barajas, Pouye Yazdi.

<sup>a</sup>ETSI Topografía, Geodesia y Cartografía, Universidad Politécnica de Madrid, Spain e-mail: sandra.mcuevas@upm.es

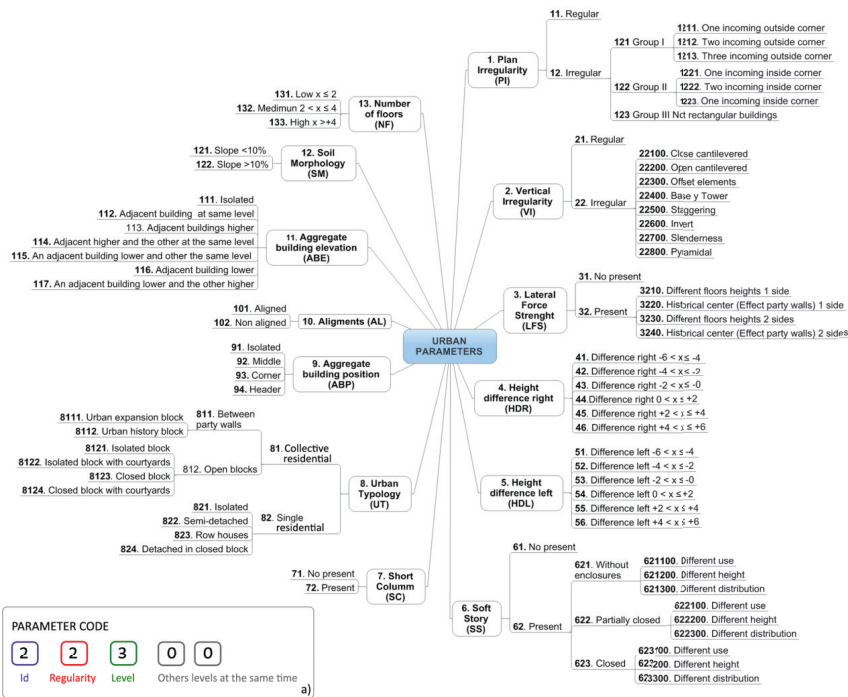


## Abstract

Despite the importance of spatial planning and urban planning in areas with seismic risk, urban parameters affecting the vulnerability of buildings have not received particular attention from researchers. Some international initiatives Benedetti and Petrini, 1984, the EMS-98 and the project Risk-UE 2003, aware of the importance of this project have pondered through behaviour modifiers, urban parameters, increasing or decreasing in this manner the final vulnerability of the building. This paper analyses urban planning in earthquake zones to obtain classification of urban parameters that make cities more vulnerable, to this end the research is based on the developments carried out within the sphere of the Risk-EU project, in its Level I empirical methodology, with the study of behaviour modifiers. This analysis should be effective in autonomous regions, municipalities, urban planners, to establish urban regulations, construct new buildings and upgrade the seismic behaviour of existing cities.

**Keywords:** Seismic vulnerability, behaviour modifiers, urban planning, damage degree.

## 1. Irregular urban parameters from an antiseismic perspective.



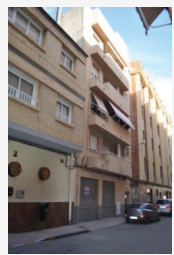
### VERTICAL IRREGULARITY



### ALIGNMENTS



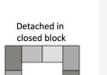
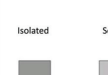
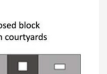
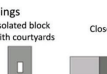
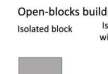
### LATERAL FORCE



### URBAN TYPOLOGY

#### COLLECTIVE RESIDENTIAL

##### Buildings between party walls



### SHORT COLUMN



## 2. Standardization of irregular urban planning parameters.

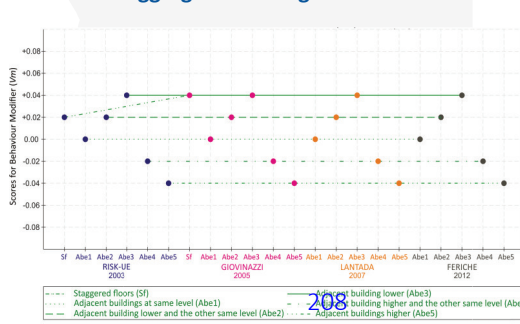
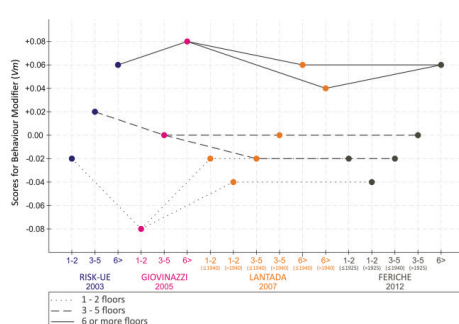
URBAN PARAMETERS	REGULATIONS GENERAL PLAN									
	TYPOLOGY	LAND USE			LAND DIVISION			VOLUME		
		Characteristic	Complementary	Compatible	Minimal plot	Minimal facade	Minimal setting back	Maximum bottom	Maximum height	Semi-basement
PI										
VI										
LFS										
HD										
SS										
SC										

## 3. Comparative analysis of the different values proposed of urban parameters

### UNREINFORCED MASONRY

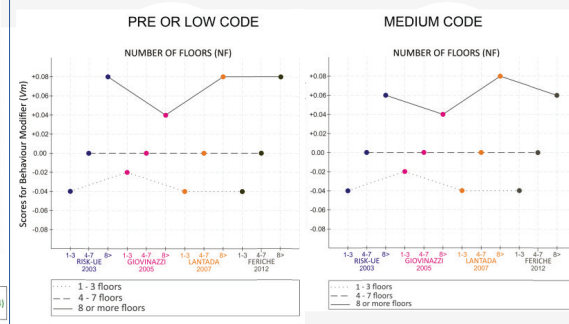
#### Number of floors

#### Aggregate building elevation



### REINFORCED CONCRETE

#### Number of floors





<sup>a</sup> Amadeo Benavent, <sup>a</sup> Santiago Félix Mota, <sup>a</sup> Oscar Villafañá, <sup>a</sup> David Galé

<sup>a</sup> Department of Mechanical Engineering, Polytechnic University of Madrid, Spain  
(amadeo.benavent@upm.es)

## Abstract

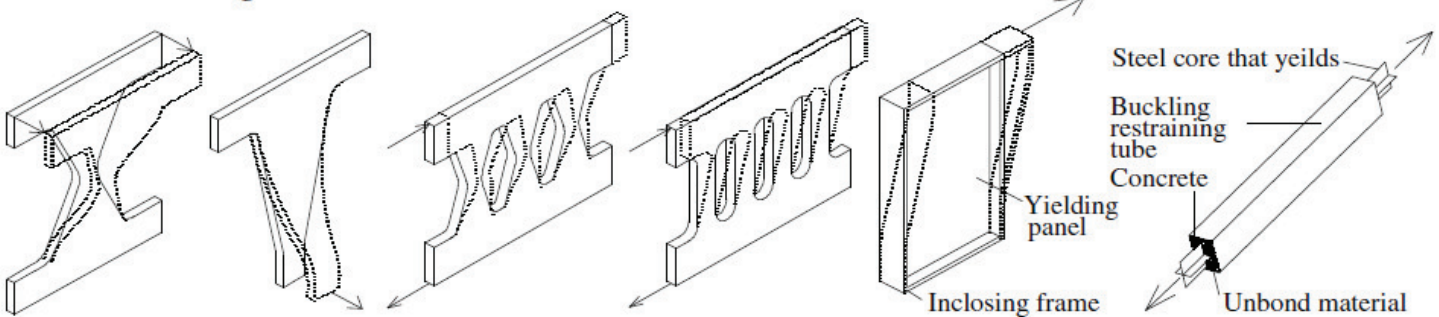
Two new type of seismic damper have been developed for passive control of structures under seismic hazard by this research group. The first type has a form of braces and it is based on yielding the web of short length segments of wide-flange or I-shaped steel section under out-of-plane bending. While the second one, most current, consist of a tube-in-tube assemblage of two commonly available hollow structural sections. The outer hollow section of the Tube-in-Tube Damper (TTD) has a series of strips creating by cutting a series of slits though the wall, and it is welded to the inner hollow section in such a way that when the brace damper is subjected to forced displacements in the direction of its axis, the strips dissipate energy through flexural/shear yielding. The hysteretic behavior and ultimate energy dissipation capacity is investigated via component test under cyclic loads for both dampers. Finally, based on the test results, a hysteric model and a procedure for predicting the ultimate energy dissipation capacity and failure of the new damper are proposed.

## Types of seismic dampers for passive control during earthquake

In contrast to the traditional seismic design approach that relies on the inelastic deformation of particular zones of the structure to dissipate most of the energy input by the earthquake (commonly, beam-ends and column-ends on moment-resisting frames), in the passive control systems this energy is delivered to special devices called seismic dampers. This has many advantages:

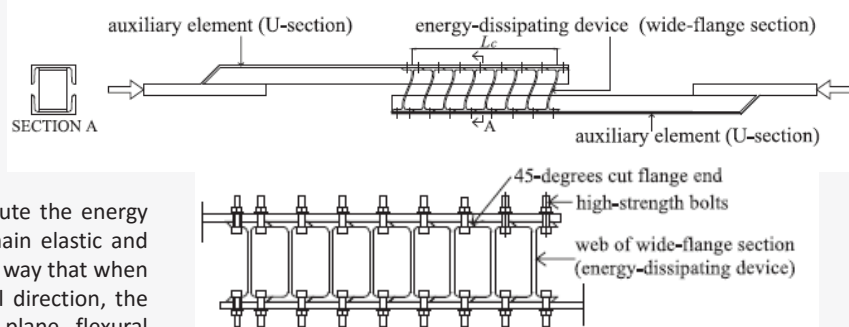
- The inelastic deformations are concentrated in the seismic dampers and the damage in the parent structure can be drastically reduced or eliminated
- The addition of damping reduces the lateral displacements of the structure, which also reduces damage to non-structural elements
- by strategically locating the seismic dampers, their inspection, repair and/or replacement following an earthquake can be carried out with minimal cost and without interrupting occupancy.

A number of mechanisms have been used for passive energy dissipation, including metal yielding, phase transformation of metals, friction sliding, fluid orificing, and deformation of viscoelastic solids or liquids. The yielding of metals is one of the most popular mechanisms and numerous metallic dampers with different yielding schemes have been proposed and installed



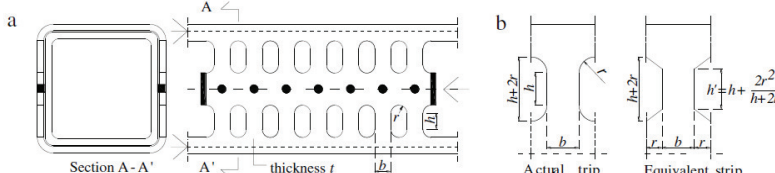
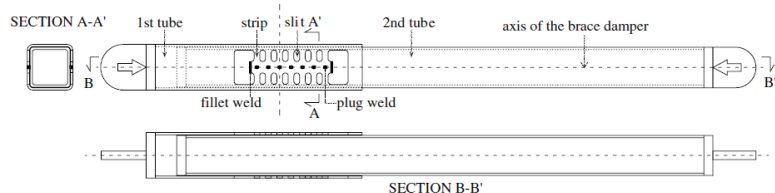
## Wide-flange section web seismic damper

The seismic damper proposed here has the form of a conventional brace, and it is intended to be installed in a framed structure as a standard diagonal bar. It is constructed by assembling several short length segments of wide-flange or I-shaped sections which constitute the energy dissipating device or damping device, and two steel bars that remain elastic and function as auxiliary elements. The assemblage is arranged in such a way that when the brace damper is subjected to forced deformations in the axial direction, the web of the wide-flange or I-shape section undergoes out-of-plane flexural deformations.



## Hollow section brace-type seismic damper

This type of seismic damper has the form and the manner of being installed as the damper explained above. However, it is constructed by assembling two standard hollow structural rectangular sections, one into the other, forming a tube-in-tube type bracing member. In the walls of the outer hollow section, a number of slits are cut leaving a number of strips between the slits. The two tubes are joined by fillet and plug welds in specific points. Under relative displacements of the ends of the brace damper in the direction of its axis, the strips behave as a series of fixed-ended beams and deform in double curvature. The tube-in-tube configuration and the overlapping length of one tube into the other increase the buckling capacity. The position of the slits along one of the tubes is not predetermined; they can be situated at the ends, or in the middle part to facilitate inspection after a seismic event.



# HOW NEW FAULT DATA AND MODELS AFFECT SEISMIC HAZARD RESULTS? EXAMPLES FROM SOUTHEAST SPAIN

J. M. Gaspar-Escribano, M.B. Benito, A. Staller, S. Ruiz Barajas,  
L.E. Quirós, P. Yazdi, S. Martínez-Cuevas, Y. Torres

Filiation: Earthquake Engineering Research Group UPM (jorge.gaspar@upm.es)



Earthquake  
Engineering  
Research  
Group UPM



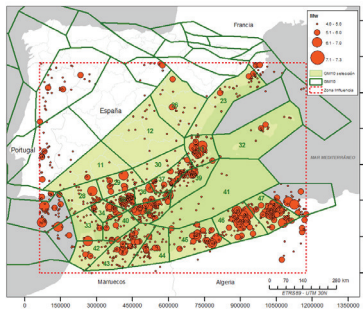
## Abstract

We study the impact of different approaches to include faults in a seismic hazard assessment analysis, with an application in Murcia (SE Spain). We use:

- Two methods to distribute the seismicity of the area into faults and area-sources, based on magnitude partitioning and on moment rate distribution.
- Two recurrence models for faults: the characteristic earthquake model and the modified Gutenberg-Richter frequency-magnitude distribution.
- Two sets of parameters to model fault recurrence periods: (i) one derived from paleoseismological and field studies obtained from the literature and online repositories and (ii) another one based on geodetically-derived slip rates for some significant faults only.

This work is part of the MERISUR project (ref. CGL2013-40492-R), with funding from the Spanish Ministerio de Economía y Competitividad.

## Source models

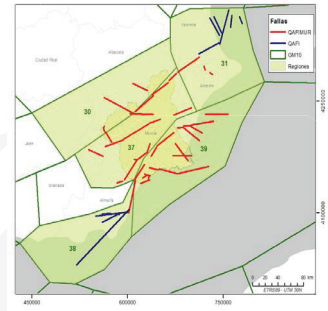


### Model 1

- ⇒ Magnitude-based.
- ⇒ Fault sources for large earthquakes, with a characteristic earthquake model (time-independent).
- ⇒ Area-sources for small earthquakes, with a modified Gutenberg-Richter recurrence model.

### Model 2

- ⇒ Moment rate-based:
- ⇒ The distribution of moment rate between faults and area-sources is derived from the catalog (in the magnitude and time intervals of completeness).



## Fault slip rates

### Geological data

- ⇒ Dating paleo earthquakes
- ⇒ Interpreting deposition / deformation patterns
- Source: [info.igme.es/qafi/](http://info.igme.es/qafi/)

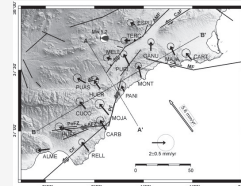


Geología 12

ID	Fault Name	Mmax	Paleoseismic		Geodetic	
			SR	RP	SR	RP
ES626	Alhama de Murcia (1/4)	6.5-7.0	0.500	3166	1.350	1173
ES627	Alhama de Murcia (2/4)	6.4-6.8	0.300	4350	1.350	967
ES628	Alhama de Murcia (3/4)	6.3-6.5	0.000	-	1.000	1023
ES629	Alhama de Murcia (4/4)	6.5-6.9	0.000	-	0.200	7257
ES609	Palomares (1/2)	6.6-7.1	0.040	65583	0.150	17489
ES630	Carboneras (1/2)	6.8-7.7	1.101	2957	1.400	2325
ES610	Palomares (2/2)	6.5-6.8	0.050	39646	0.150	13215

### Geodetic data

- ⇒ Deformation derived from precise GPS measurements of stations along years.



Echeverría et al. 2013

## Hazard maps: Sensitivity analysis

### Sensitivity to models and slip rates

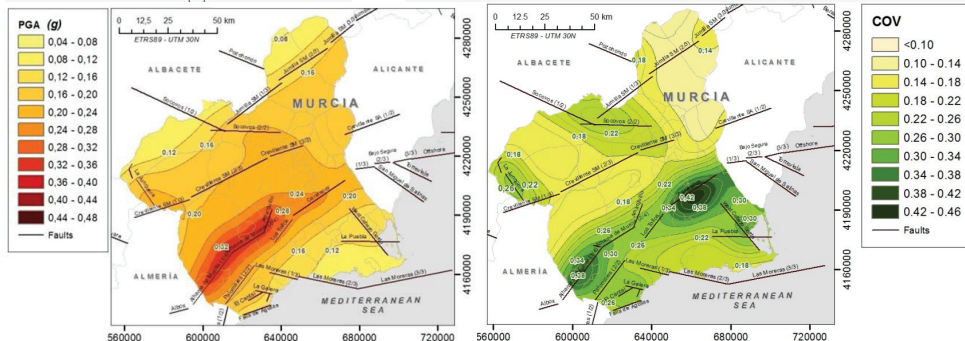
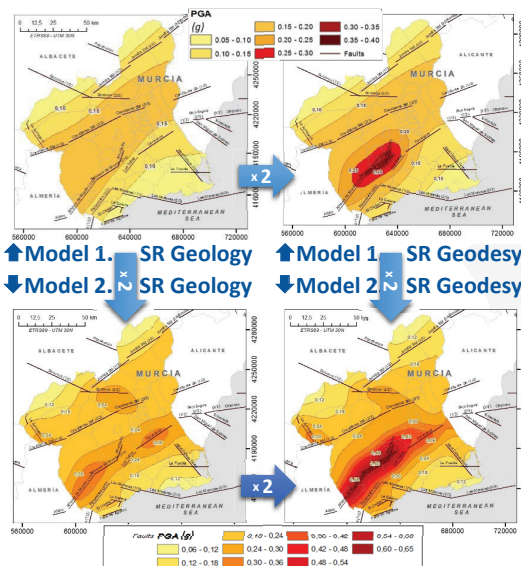
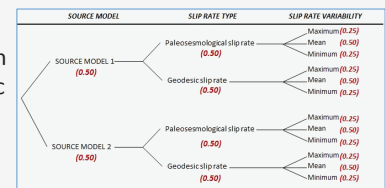
#### Up to 4 times difference !

- ⇒ Model 2 gives larger PGA values than Model 1 around faults.
- ⇒ Geodetic slip rates are larger than geological slip rates, resulting in larger hazard estimates.

### Overall variability

- ⇒ The weighted mean of the PGA estimates obtained with models 1 and 2 and the slip rates derived from geodetic and paleoseismic data is represented in a map.
- ⇒ COV values are large around fault areas, indicating a large variability of results to different input choices.

### Logic tree and weights



## Conclusions

- ⇒ Different models of seismic source characterization including faults as independent sources are tested in the region of Spain with the best data availability.
- ⇒ The larger amount of data does not lead to a reduction of epistemic uncertainty.
- ⇒ Thus, a large variability on hazard results to different input choices is observed.



Belén Benito<sup>1</sup>, Alicia Rivas<sup>1</sup>, Jorge M. Gaspar-Escribano<sup>1</sup>, Alejandra Staller<sup>1</sup>, Sandra Ruiz Barajas<sup>1</sup>, Ligia-Elena Quirós<sup>1</sup>, Pouye Yazdi<sup>1</sup>, Sandra Martínez-Cuevas<sup>1</sup>, Yolanda Torres<sup>1</sup>

<sup>a</sup>Corresponding author : Belén Benito, 1. ETSI Topografía, Geodesia y Cartografía (mariabelen.benito@upm.es)

## Abstract

A new estimation of seismic hazard has been developed for the Spanish territory aimed at the revision of the Spanish Building Code. The study includes geologic, seismic and strong motion data gathered in the last years, being remarkable the use of: 1) the Data Base of Quaternary Active Faults of Iberia (QAFI,v2) an updated seismic catalogue homogenized to Mw, 3) a new area-source model compiling different geophysical data and 4) a ground motion prediction equation derived with local data, covering the magnitude Mw range (4-5.5). Its worthy to note the information and lessons derived from the Lorca 2011 earthquake, which has been the most destructive event in the last 120 years in Spain.

A probabilistic seismic hazard approach has been followed (PSHA) joining the consensus of the main specialists of the country who have participated in the decisions around the critical aspects, such as: source model and GMPE to be used for different magnitude ranges, values of maximum magnitude  $M_{max}$  for each zone, logic tree and weights for uncertainty quantification, etc. As result, hazard maps in terms of PGA and spectral accelerations SA (T) have been obtained for different return periods: 475, 975 and 2475 years. The new hazard maps counts with the agreement of the Spanish seismological community and are presented in this communication.

## 1. Seismic Hazard Approach

The seismic-hazard analysis has been carried out according to the well-known probabilistic seismic-hazard assessment (PSHA) approach with two variants: zoned and zoneless methods. To take into account the epistemic uncertainties linked to different stages of the process, a logic tree was formulated, while the aleatory uncertainties have been considered through Monte Carlo simulation. The necessary inputs for the application of the zoned method have been prepared in the first phase of hazard estimation: 1. Seismic catalogue, 2. Zoning models and seismic parameters, 3. Ground motion prediction Equations (GMPEs).

### 1.1. Seismic Catalogue

The seismic catalogue has been homogenized to moment magnitude Mw and contains 6999 events in the ranges of magnitude Mw (3.5-8.5), depth (0-65 km) and covering the period (1048-June 2011). Figure 1 shows the epicenters of the final project catalogue.

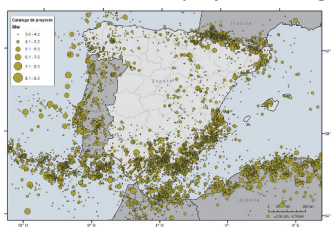


Figura 1.- Epicenters of the earthquakes contained in the project catalogue

### 1.2. Zoning Models and seismic parameters

Model of seismogenic zones proposed by Garcia Mayordomo et al (2012) and Bernal et al (2012) have been choosing for applying the zoned method. As example, Figure 2 shows the first one, named GM12. The seismic parameters for each zone have been obtained fitting the seismicity to a Gutenberg-Richter law. The maximum expected magnitude,  $M_{max}$ , has been derived from the faults contained in the QAFI Data Base (Quaternary faults of the Iberian Peninsula, Figure 3).

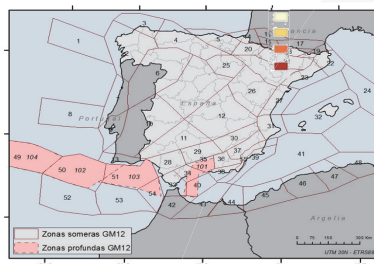


Figura 2.- Zonation of GM12

### Maximun Magnitud (Mmax)

In Spanish Peninsular territory  $M_{max} \approx 6.5-6.8$  in South-East Spain (Almeria, Alicante, Murcia, Granada):

In Azores Gibraltar  $M_{max} = 8.5$ .

Figura 3.- Quaternary active faults of Iberia (QAFI DB)



### 1.3. Ground Motion Prediction Equations (GMPE)

Different GMPE have been used, reflecting the attenuation in two tectonic regimes:

- 1) Active surface crust of the Iberian Peninsula and North Africa. Mw [4-7]
- 2) Deep zones (Alboran) and tectonic regime of Azores-Gibraltar, Mw [4-8.5].

A new local attenuation model has been derived from 140 accelerograms of Spain, corresponding to Mw magnitudes [4 - 5] and distances up to 340 km.

## 2. Results , conclusions and discussion

A set of maps for different ground motion parameters and return periods has been obtained, included in IGN-UPM (2012). Figure 4, shows the new map of PGA (on rock) for return period of 475 year (10 % exceedance probability in 50 years), to be used for the revision of the Spanish Building code NCSE-02.

Following results are remarkable:

- Maximum values of PGA=0.24 g in Granada and Bajo Segura Basin
- PGA > 0.08g in most part of Andalusia, Murcia, Comunidad Valenciana, Navarra, Huesca and Catalonia.
- PGA < 0.04 g in Meseta Central and part of the Ebro Basin
- The maps of the building codes for France and Portugal are also represented in the boundaries.

Figure 5 shows the differences between the new and the NCSE-02 maps. The biggest increments, around 0.1 a 0.13 g, are found in some parts of Andalusia, Murcia, Alicante, Valencia and Pyrenees. In general the seismic hazard increases according the new map, with minor differences in central part of Spain. The area where PGA < 0.04 g, in which building design is no required (according NCSE-02) is reduced in the new map.

The increment of the hazard obtained in this study reflects a mayor convergence with the hazard maps of French and Portugal in the boundaries.

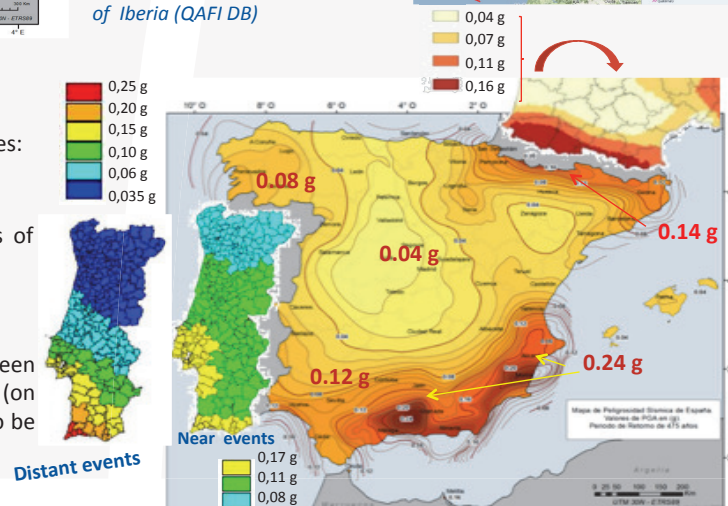


Figure 4. New Hazard map of Spain, PGA for return period of 475 years. The maps of the building codes of France and Portugal are also represented in the boundaries. In the case of Portugal, 2 maps are included: left) for the action of the distant Atlantic earthquakes and right) hazard due to the near Peninsular shocks.

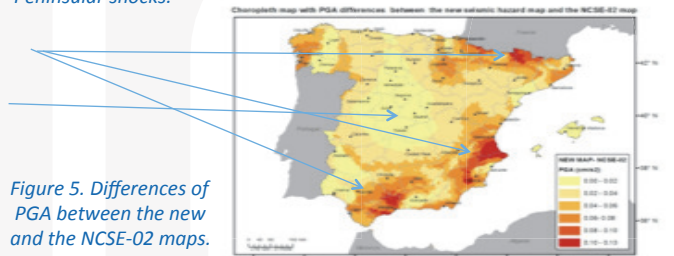


Figure 5. Differences of PGA between the new and the NCSE-02 maps.





## Vehicles and Railways

- |            |     |   |
|------------|-----|---|
| [VEH - 01] | 215 | <i>"Accuracy improvement of finite element models of electric vehicles components manufactured with thermoplastic materials in crash environments."</i> Rivera, Javier; Martínez, Luis; García, Antonio.            |
| [VEH - 02] | 216 | <i>"Analysis and Development of Storage Systems for Electric Vehicles (EV) and Impact Evaluation of EV Integration on Distribution Networks."</i> Nájera, Jorge; Rodríguez, Jaime; de Castro, Rosa M <sup>a</sup> . |
| [VEH - 03] | 217 | <i>"Large-signal modeling of bidirectional battery charger for electric vehicles. System-level approach based on agent-based models in V2G environment."</i> Naziris, Antreas; Asensi, Rafael; Uceda, Javier.       |
| [VEH - 04] | 218 | <i>"Management Strategies for Electric Vehicle."</i> Alvaro-Hermana, Roberto; Fraile-Ardanuy, Jesus; Martinez, Sergio.  |
| [VEH - 05] | 219 | <i>"A co-simulation environment for cooperative maneuvers among vehicles."</i> Artuñedo, Antonio; Haber, Rodolfo; Matía, Fernando.  |
| [VEH - 06] | 220 | <i>"Methodology for measurement of energy expenditure when getting in and out of a car using the motion capture system Kinect."</i> Martínez, Francisco.  |
| [VEH - 07] | 221 | <i>"Electric Vehicle Cluster: Charging Infrastructure Development for Electric Car",</i> Nogueras, Javier Cano; Martínez-Val, José María; San Millán, Julio.  |
| [VEH - 08] | 222 | <i>"Smart modelling for planning, design and protection of high-performance rail networks."</i> Calvo, Álvaro.  |
| [VEH - 09] | 223 | <i>"Soil Structure Interaction in Underpasses Structures due to High-speed Trains."</i> Báez, Manuel F.; Fraile, Alberto.   |



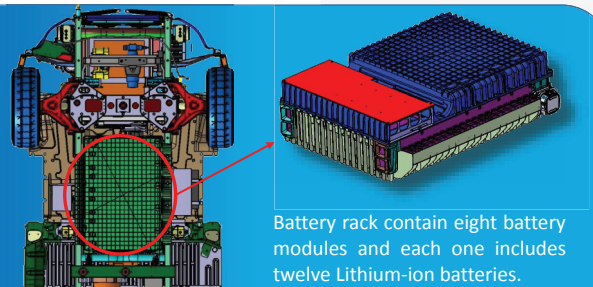


## Abstract.

Currently, the weight reduction in the vehicle is a primary objective, especially in hybrid and electric vehicles because these type of vehicles have an extra mass due to the batteries. In this context, the use of plastic materials in structural elements for weight reduction represents a technological challenge. The present work is focused on the development of a methodology to improve the accuracy of the virtual tests results of structural large plastic components, with high level of additives, when these parts have to withstand high levels of dynamic loads like vehicle crashes. For the development of the proposed methodology, the design of battery rack on the OPERA4FEV project (FP7) is used. The OPERA4FEV rack is manufactured in a thermoplastic material with fibre glass reinforced and flame retardant additives. These type of racks have to withstand crash load as defined in the United Nations regulation 100. For the design of this rack, finite elements simulations and traditional tests have been used. Finally, the research work carried out has helped in designing a more efficient battery rack from the energy point of view (with a mass reduction greater than 20% compared to traditional solutions) and using eco-design materials.

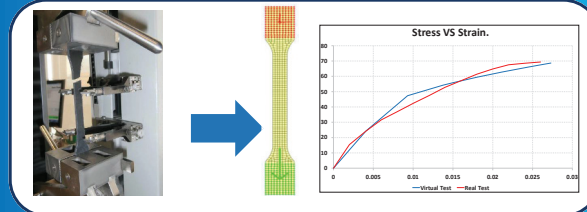
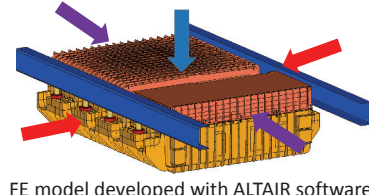
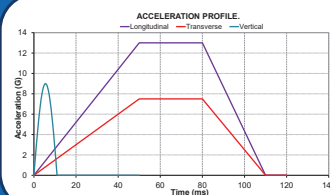
## Objectives.

- Establish a methodology to improve finite elements models accuracy to perform virtual crash test of large components manufactured in thermoplastic materials with high degree of additives.
- Obtain the suitable parameters of thermoplastic material properties in large models which are used in explicit finite elements models.
- Guarantee that a thermoplastic battery rack design supports crash loads.



## Methodology.

**Stage 1:** Analysis of the thermoplastic material behaviour subject to the strain rate and temperature influence. The ALTAIR-RADIOSS software is being used for simulation in several velocity conditions.



**Stage 2:** Virtual test simulations according with Regulation 100 recommendations and overload acceleration pulses in five directions (frontal, rear, both sides lateral and vertical).

**Stage 3:** Comparison between the virtual test results and the real crash test results using the information obtained at several load severities and impact directions.

**Stage 4:** Obtain conclusions and virtual OPERA4FEV battery rack validation.



## Currently status.

The thermoplastic material characterization has being optimized through the virtual tensile tests with the material parameters variation on the mathematical model Johnson Cook. The objective is to improve the approximation of the stress-strain curve obtained in the virtual tensile tests with respect to the information of the real crash tests with physical specimens.

In parallel, the dynamic forces effects on large plastic components are simulated. The model results are compared with the real crash tests to find the differences and similarities between both cases.

## Further work.

- Reduce the error due to the mathematical formulation, in the finite element model on the virtual crash test, of the large plastic components.
- Refine the virtual tests prediction accuracy using the standard load and overload results of the real crash tests.
- Quantify the error contribution of other factors (no related to the material formulation), using the final virtual tests results compared to the real crash results.
- To apply developed capabilities to other vehicle parts.

## ACKNOWLEDGMENTS.

This work was financially supported by the European Commission, in the framework of the project OPERA4FEV inside the FP7-2011-GC-Electrochemical Storage Programme with contract number SCP1-GA-2011-285671. Part of this research was funded by the Comunidad de Madrid through the SEGVAUTOTRIES, Seguridad de los vehículos Automóviles, por un Transporte Inteligente, Eficiente y Seguro, with contract number S2013/MIT-2713.

# Analysis and Development of Storage Systems for Electric Vehicles (EV) and Impact Evaluation of EV Integration on Distribution Networks

**Jorge Nájera, Jaime Rodríguez, Rosa M<sup>a</sup> De Castro**  
Department of Electrical Engineering, ETSI Industriales, UPM  
(jorge.najera.alvarez@alumnos.upm.es)

## Abstract

Electric Vehicle (EV) integration on Distribution Networks has been thoroughly studied over the past 10 years, and it is widely agreed that an intelligent integration can yield benefits to the EV owner, the power grid and society. Despite this fact, EV battery lifespan has become a crucial issue when speaking about EVs. Due to the expensiveness of batteries, EV owners expect them to last long periods of time. Lithium-Ion (Li-ion) batteries have emerged as the major power source for EVs, and their lifespan and performance is closely related to the quality of the charging pattern. Numerous battery charging controllers have been developed and tested proving that, depending on the EV penetration, it is possible to fulfill the network requirements in terms of reliability and quality by keeping the EV batteries charging pattern under control. Nevertheless, a scenario where EV owners would accept having an EV charging power limited by a controller is far from the reality, because the majority of owners are intent on having their batteries fully charged as fast as possible. Due to this fact, this project aims to analyze, study and develop a methodology to calculate charging patterns that satisfy the needs of EV owners and the requirements of the grid, as well as extend the batteries' lifespan.

Therefore, a detailed simulation model of the Li-ion battery and electrical bench, which allows to charge and discharge the batteries in the laboratory, will be developed, as well as an algorithm to find the optimum charging pattern. The obtained results will be tested on real Li-ion batteries. Moreover, an economic and technical study will be performed with the changes that would be necessary to implement in different networks adapting them to the increasing EV penetration.

## Analysis and Development of Storage Systems for Electric Vehicles and Impact Evaluation of Electric Vehicle Integration on Distribution Networks

The electrical bench with the required equipment for performing different battery tests has been modelled in MATLAB Simulink SimPowerSystems. Furthermore, multiple benchmark networks have also been modelled in MATLAB. The electrical bench scheme and a single-line diagram of one of the benchmark low voltage grids can be seen in the following images:

The electrical bench is formed by a transformer, two sets of inductances and two converters, controlled by a DSP. DC/AC converter is controlled with a SVPWM strategy, and the control variables are the DC voltage and the reactive current interchanged with the grid. DC/DC converter divides the DC current between the three branches. Each branch is controlled with a PWM strategy with a lag of 1/3 of the triangular modulating wave period between each branch, so the harmonic distortion originated by the converter is diminished. This DC/DC converter disposition is called "interleave".

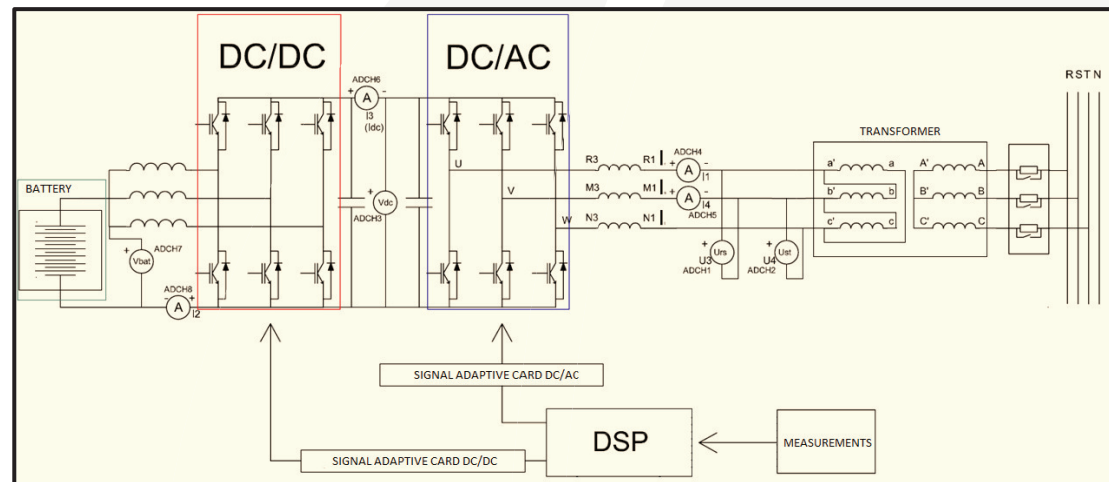


Figure 1. Schematic representation of the modelled electrical bench for battery testing.

Cigrè Benchmark Low Voltage network is one of the grids that will be taken into consideration when it comes to evaluating EV penetration. Figure 2 shows that this network has three different branches, corresponding to Residential, Industrial and Commercial loads. This disposition allows the testing of EV battery charging patterns in residential charging stations, which are usually designed for slow charging rates, together with bigger commercial installations that charge the battery at higher rates.

Moreover, the modelled networks will be used to evaluate the grid behavior against the imbalances and the harmonic distortion induced by EVs, two great concerns for proper distribution network performance.

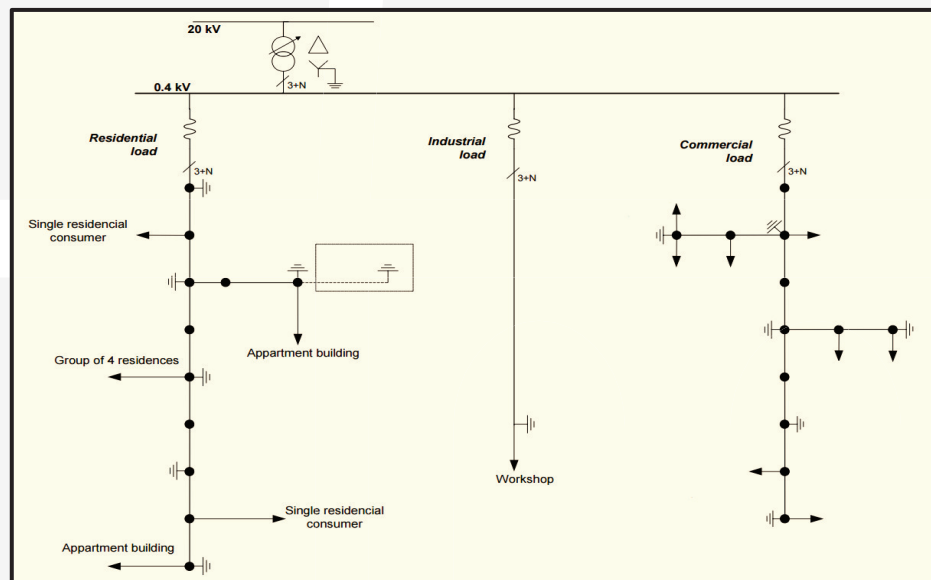


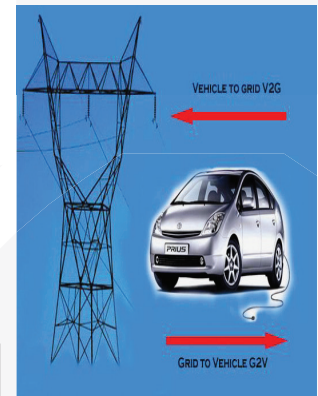
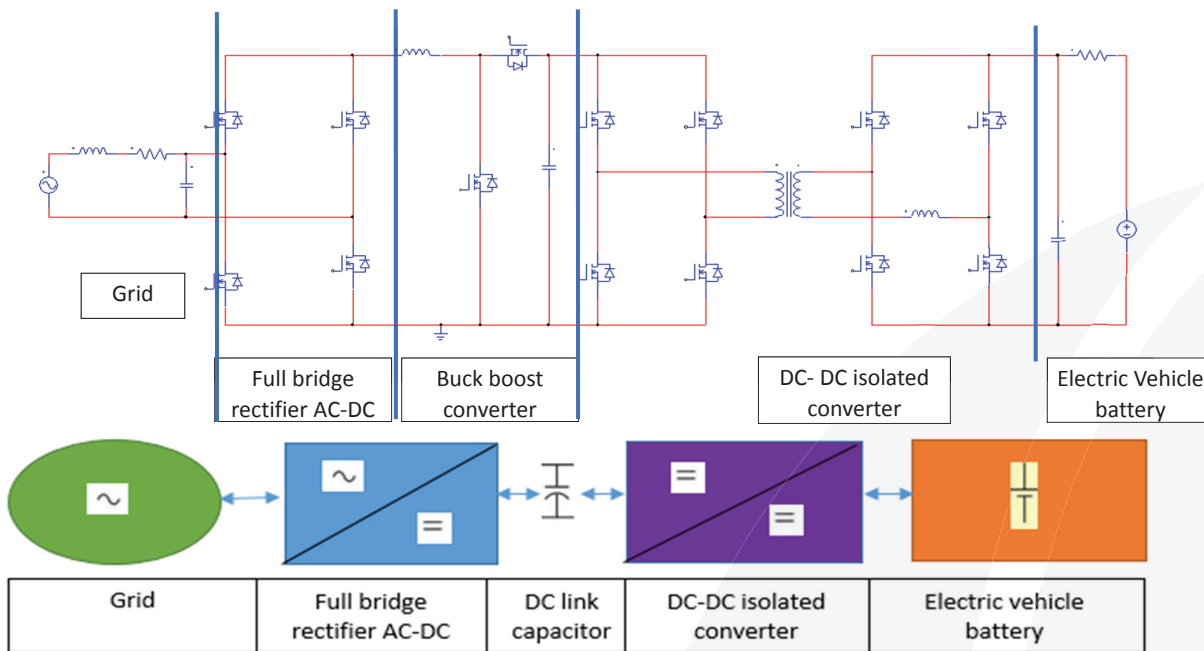
Figure 2. Single-line diagram of Cigrè Benchmark Low Voltage network.



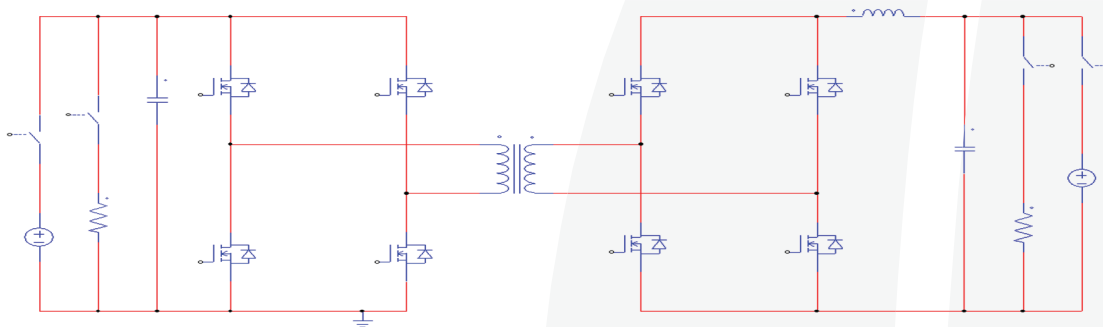
## Abstract

The purpose of this work is the development of a model able to work at system level, studying the impact of the connection to the grid of a number of electric vehicles demanding energy from the grid to charge their batteries, but at the same time the grid operator may use the energy stored in the batteries for optimal energy management at system-level. At the beginning a large-signal model of a bi-directional battery charger is developed to foresee the converter behaviour. Later, at system level an Agent-based model will be developed to assess the system performance, specially in micro-grids.

## Proposed system



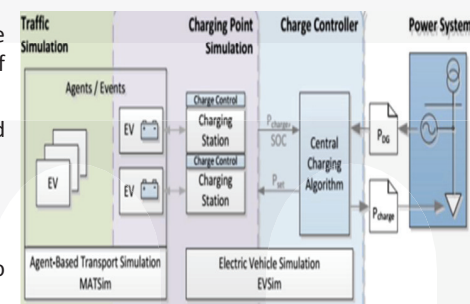
## Bidirectional DC-DC Converter



## Multi-agent modelling

By having thousands of potential EV, traffic conditions, charging stations, grid operating conditions, the level of complexity is so high, that we need modelling techniques compatible to deal with such level of complexity:

- Multi agent modelling tool allow us to identify individual agents through their characteristics and behaviours
- Combination of agents with the ability to cooperate, to act autonomously and to learn
- Interactions in a complex environment let us to simulate the behaviour of such complex systems
- Develops the simulation environment able to foresee the performance of the grid for the operators, to define the charging strategy for EV fleets



## Future work

- Show the results of large-signal model for bi-directional battery chargers using a black-box approach
- Introduce the multi-agent modelling in the case of vast amount of Electric Vehicles in the system

## Abstract

The research leading to these results has received funding from the EU 7<sup>th</sup> FP under the project DATA science for SIMulating the era of electric vehicles (DATASIM, FP7-ICT-270833). DATA SIM aims at providing an entirely new and highly detailed spatial-temporal microsimulation methodology for human mobility with the goal to forecast the nation-wide consequences of a massive switch to electric vehicles. The objective of this work is focused in the development of charging management strategies for electric vehicle (EV) fleets. Its purpose is to maximize the integration of EVs in the current electric grid considering their consumption and their charging limits, both temporal and spatially. The main contribution of this work is the development of a novel Peer to Peer Energy Trading System (P2PETS) between EVs in order to reduce the impact of charging EVs over the electric grid.

## P2P Energy Trading System

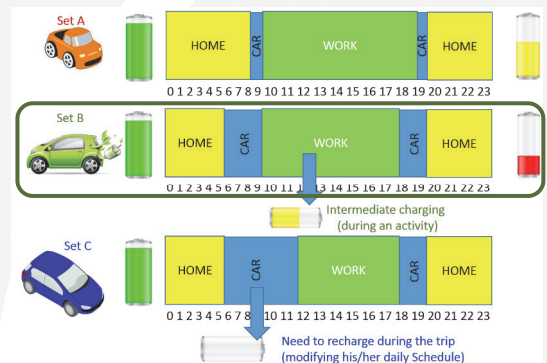
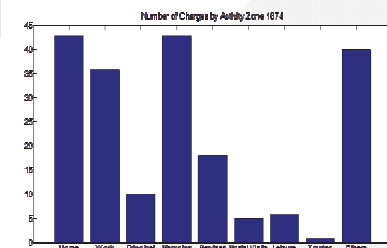
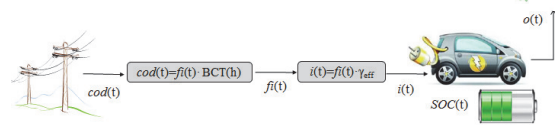
### Activity Based Mobility Model & Driver Classification

The temporal and spatial behavior of EVs is modeled using an activity-based (AB) micro-simulation model that predicts the daily scheduled activities for each member of a synthetic population in Flanders region (Belgium). This region is divided in 2368 different traffic analysis zones (TAZ) and a complete schedule list for the whole population is obtained, allowing to know for each member of this population when, where and which activities are done and the transportation mode used (by foot, by train, by car, etc.).

Based on this AB model, all current car drivers in Flanders region have been classified in three different sets according to their daily consumption.

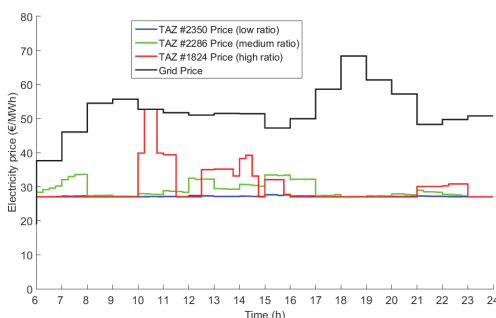
### Charging cost and location

For each driver from set B, the optimal charging cost is calculated. For each zone, the activities performed by the drivers while charging are also evaluated.

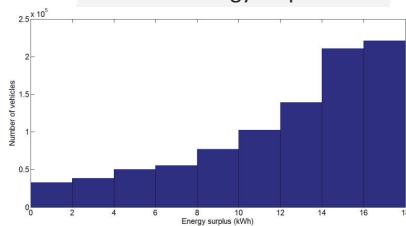


### P2P Electricity market

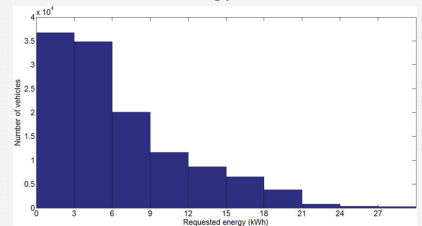
- A P2P trading system that interconnects both market actors: vehicles with an energy surplus at the end of the day (set A) and vehicles demanding extra energy along the day (set B).
- An aggregator sets the energy and the price to be given to set A vehicles depending on demand, energy stored in set A vehicles and grid price.
- P2P electricity price highly depends on ratio between set B and set A vehicles. This ratio is usually low.
- Total charging costs for both vehicles sets is diminished. The P2P Energy Trading System is day-charging independent.



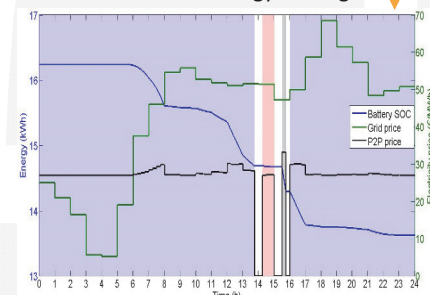
Set A: Energy surplus



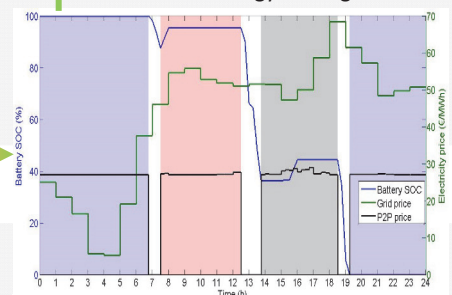
Set B: Energy demand



Set A: P2P Energy trading



Set B: P2P Energy trading



R. Alvaro, J. Gonzalez, J. Fraile-Ardanuy, P. Zufiria, L. Knapen, D. Janssens, "Peer to Peer Energy Trading with Electric Vehicles," IEEE Intelligent Transportation Systems Magazine, Accepted.

R. Alvaro, J. Fraile-Ardanuy, "Charge scheduling strategies for managing an electric vehicle fleet parking," in 2015 - IEEE International Conference on Computer as a Tool, 8-11 Sept. 2015. doi: 10.1109/EUROCON.2015.7313732.

R. Alvaro, J. Gonzalez, C. Gamallo, J. Fraile-Ardanuy, L. Knapen, "Vehicle to vehicle energy exchange in smart grid applications," in 2014 International Conference on Connected Vehicles and Expo (ICCVE), pp. 178-184, 3-7 Nov. 2014. doi: 10.1109/ICCVE.2014.7297538.

J. Gonzalez, R. Alvaro, C. Gamallo, M. Fuentes, J. Fraile-Ardanuy, L. Knapen, D. Janssens, "Determining Electric Vehicle Charging Point Locations Considering Drivers' Daily Activities," Procedia Computer Science, vol. 32, 2014, pp. 647-654, doi: 10.1016/j.procs.2014.05.472.

R. Alvaro, J. Gonzalez, J. Fraile-Ardanuy, L. Knapen, D. Janssens, "Nationwide impact and vehicle to grid application of electric vehicles mobility using an activity based model," in 2013 International Conference on Renewable Energy Research and Applications (ICRERA), pp. 857-861, 20-23 Oct. 2013. doi: 10.1109/ICRERA.2013.6749871.

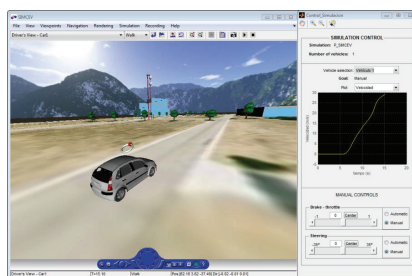
C. Gamallo, R. Alvaro, J. Fraile-Ardanuy, M. Fuentes, "Evaluation of the utilization of electric vehicles for building energy management in hotels," in New Concepts in 2013 International Conference on Smart Cities: Fostering Public and Private Alliances (SmartMILE), 11-13 Dec. 2013. doi: 10.1109/SmartMILE.2013.6708193.

## Abstract

In this work we propose a tool for simulation of cooperative maneuvers among autonomous vehicles in which virtual and real vehicles can conjunctively interact. It is a generic simulation platform where the user can define the desired scenario using a graphical user interface. This interface facilitates insertion of controllers and models for different parts of vehicles and some elements of the infrastructure. Furthermore, vehicle to vehicle (V2V) and vehicle to infrastructure (V2I) communications are available in the framework. The simulator also enables the 3D rendering of simulation and monitoring of several variables at runtime. The main advantage of the proposed framework relies on the use of hybrid simulation by combining real and virtual vehicles for studying their dynamic behavior and interaction without the need of real expensive equipment or vehicles. Therefore, the emulation of experimental tests based on data sets from the vehicle sensors serves as a powerful tool for designing and evaluation new ADAS.

## Introduction

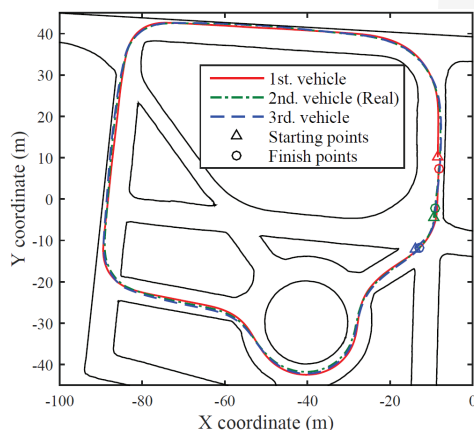
A tool for simulating a wide range of ITS applications is proposed in this work. This is a framework for simulating cooperative maneuvering among vehicles (real and virtual). The main goal is to address the new needs on ITS simulation such as ADAS, intelligent sensors simulation and testing of reliability and safety of controllers for autonomous vehicles, maintaining a balance between vehicle dynamics simulators and microscopic traffic simulators. Our proposal addresses the gap between traffic simulators and vehicle dynamics simulators allowing ITS researchers and developers to test on board vehicle equipment such as sensors, actuators or controllers, and cooperative transport maneuvers within urban realistic scenarios. The real-virtual interaction allows to combine real vehicles with simulated scenarios, therefore it is possible to evaluate the performance of the real vehicle in critical situations without jeopardizing the vehicles or the infrastructure.



## Results

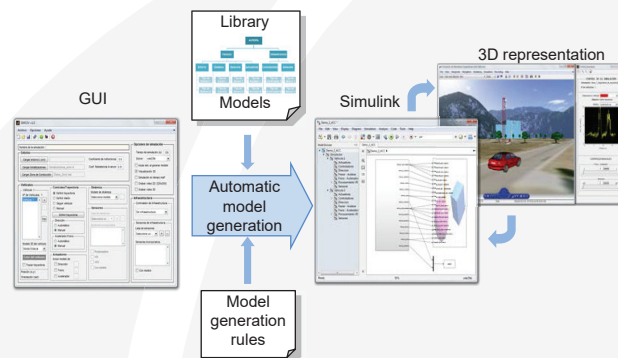
In order to analyze the result obtained with the simulation platform and validate the simulation model of the vehicle, several experiments were carried out. In these experiments a real car was used. The real vehicle is a Citroën C3 which has been adapted for autonomous driving, including several sensors such as GPS, camera and inertial measurement unit (IMU); and actuators for controlling the throttle, brake, steering wheel and gearbox. The vehicle also counts with an On-Board Unit (OBU), which is in charge of the control of the vehicle and an IEEE 802.11p communication system for V2I and V2V communications.

The results of the test demonstrated that the cooperation between simulation and real vehicles is possible, maintaining a good performance between the simulated and real systems.

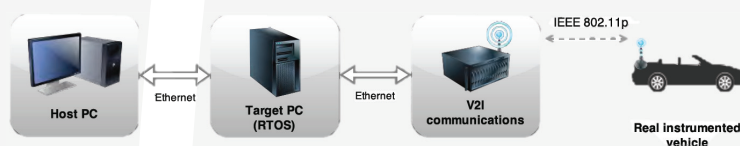


## Framework description

It is a generic simulation platform where the user can define the desired scenario using a graphical user interface, generate automatically a simulation model and then simulate it. The interface facilitates the insertion of controllers and models for different parts of vehicles and some elements of the infrastructure, through a models library. Furthermore, the framework permits to implement V2V and V2I communication links among the entities that comprise the scenario (real or simulated).



The simulator also enables the 3D rendering of simulation and monitoring of several variables at run-time. This tool uses hybrid simulation by combining real and virtual vehicles for studying their cooperative behavior without the need of real expensive equipment and vehicles. This tool also allows the recreation of experimental tests based on data sets stored from vehicle sensors. The real-virtual vehicles interaction provides new features and extends the capabilities of the framework.



## Conclusions

As proven, the tool proposes a co-simulation framework for the development of applications on the autonomous driving field. The tool has a modular structure, allowing the user to implement several models and components at different levels of the simulation environment. The simulator also enables the 3D rendering of simulation and monitoring of several variables at run-time. It makes possible real-time interaction between real and simulated cars allowing them to cooperate. Also this functionality enables to use the simulation framework as a hardware abstraction layer between hardware and control systems. Ongoing research focus on the use of this feature for developing and testing Cyber-Physical Systems in the ITS scope.

Future work will be focused on improving models of vehicle, sensors, actuators and controllers as well as the simulation of wireless systems for V2X communication systems.



## Abstract

This project aims to develop a methodology for measuring the energy expenditure of a person when getting in and out of a car. In order to capture the person's movements, the most recent specification of the motion capture system Kinect is used. The measurement of the energy expenditure is planned as a way for evaluating the accessibility to the different seats of a vehicle and is specially oriented to elderly and reduced mobility people.

Firstly, the performance of the motion capture system Kinect should be evaluated. It is necessary to determine the tracking precision of the different body joints not only in obstacle free spaces but also in spaces with visual obstacles.

Then, evaluate the capability for capturing the movements getting in the car and solve the problems caused by working in a reduced dimensions cabin with elements such as the seats and the dashboard. In addition to the motion capture, a methodology for measuring the energy expenditure of body motion and static positions should be designed.

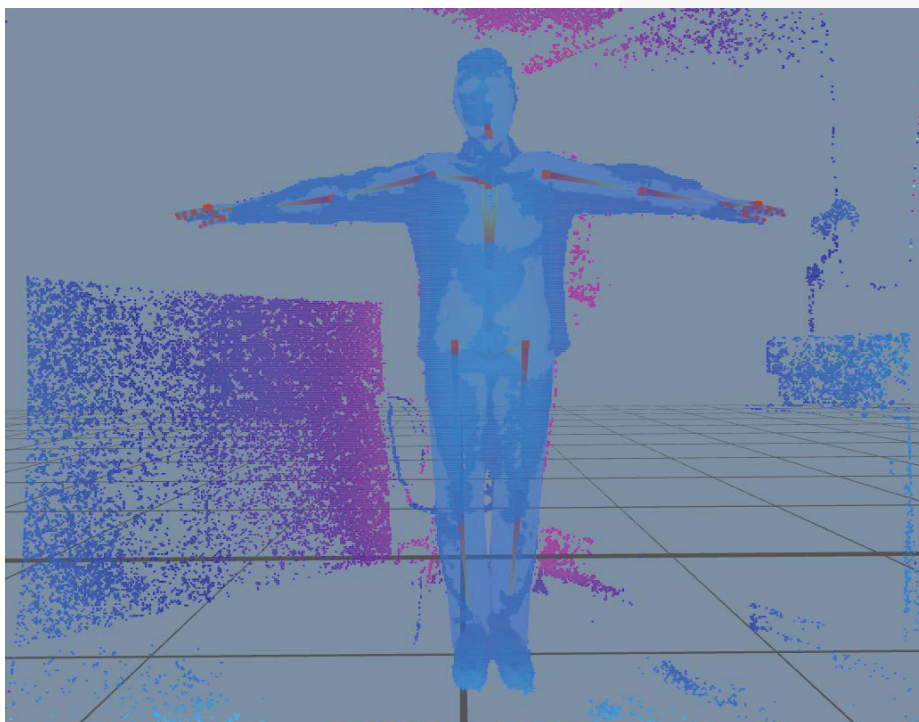
The final aim is applying this methodology and the motion capture system to different vehicles from city cars to MPVs and rate their accessibility.

## Kinect System

Kinect is a motion capture system initially designed for Xbox 360, Microsoft home videogame console. The most recent version, Kinect v2 was launched in 2014 adapted to the new video game console Xbox One.

The system includes a 1080p @ 30fps resolution color camera and a 512x424 pixel infrared depth sensor with a range between 0.5 and 4.5 m. The system has 70 degrees horizontal and 60 degrees vertical vision field. Kinect can track up to 6 complete skeleton at once, compared with 2 of its predecessor, with a greater number of joints in each skeleton, 26 versus 20.

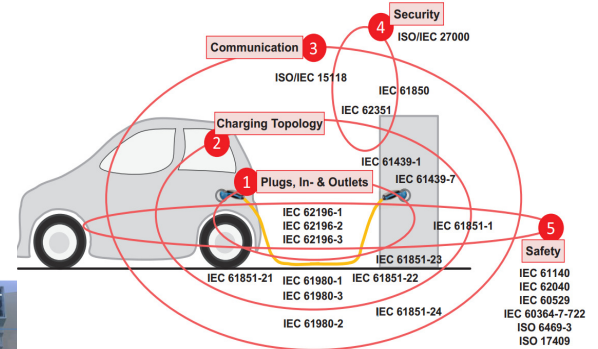
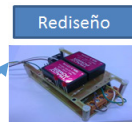
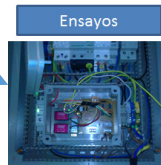
For PC use, it is available an adapter with USB 3.0 and power supply connectors.



**Javier Cano Nogueras, José María Martínez-Val, Julio San Millán**  
Oficina Técnica y Jefatura de Nuevas instalaciones de la FFII  
Universidad Politécnica de Madrid ETSI Industriales (jcano@ffii.es)

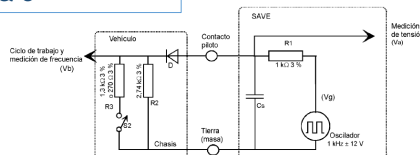
## Abstract

- Project dedicated to develop recharging infrastructure for the FFII / ETSII / UPM environment and promotion of electric vehicles use. Study of the UNE EN 61851 and UNE EN 62196, Mode 3 EVSE prototype development .
  - Electric vehicle charging station mode 3, prototipe development
  - prototype testand verification
  - Redesign , encapsulated and small production
  - Deployment of charging network in FFII -ETSII
    - Tecnogetafe
    - Insia (Campus Sur)
    - private facilities



### Pilot function

PWM modulation. Square wave. charge mode 2 & 3



### functions:

- Verification that the car is properly connected.
- Continuous integrity check protective earth conductor
- Activation system.
- Deactivation system.

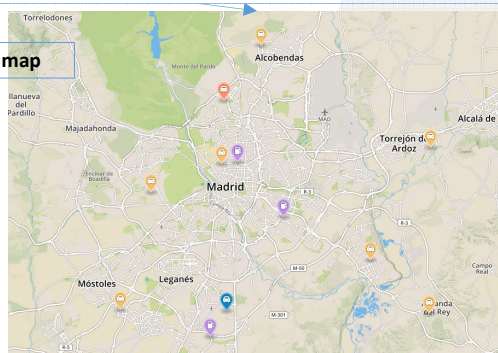
### Safety aspects provides by EVSE

- Pines without energy until negotiation EVSE-VE
- Ground fault interrupter system.
- Detección y verificación de señal piloto

### Deployment of charging network

- ETSII – 4 Charging station (J1772 230Vac 30 A)
- INSIA (Campus Sur) – One charging station 230Vac 30 A)
- Tecnogetafe
  - One experimental charging station (J1772 230Vac 30 A)
  - 3 charging station 1x J1772 230Vac 30 A & 2 J1772 230Vac 20 A )
  - 1 charging station (Mennekes 230Vac 30 A)
- Private facilities- 8 x charging station from 12 to 16 Amps.

### Charging station updated map



### Conclusions

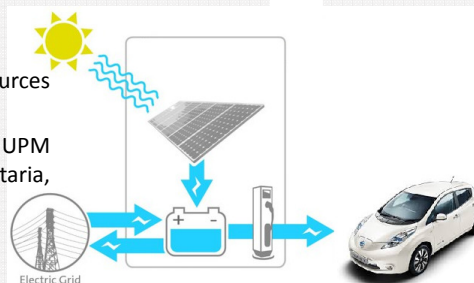
- Total availability and electrical mobility of people who are part of the cluster has been provided.
- The installations has a very high degree of availability, very low failure rate and a very low maintenance are needed
- More than 16MWh provided by the charging station network for a year, that is more than 95.000Km on electric vehicle and a reduction in CO2 emissions of over 65% (considering the Spanish electricity mix 2015)

## Future Work

Infrastructure optimization with available resources applied to recharge the electric car.

Deployment of charging network to the rest of UPM campus and centers: Ciudad Universitaria, Montegancedo...

Fast Charge station development.



## Sources:

- AENOR- UNE-EN** <http://www.aenor.es/>  
IEC 61851- Electric vehicle conductive charging system -- Part 22: AC electric vehicle charging station  
IEC 62196 - Plugs, socket-outlets, vehicle connectors and vehicle inlets - Conductive charging of electric vehicles - Part 1: General requirements.
- IDAE.**  
[http://www.idae.es/uploads/documentos/documentos\\_12144\\_G003\\_VE\\_para\\_flotas\\_2012\\_f3176e30.pdf](http://www.idae.es/uploads/documentos/documentos_12144_G003_VE_para_flotas_2012_f3176e30.pdf)
- JCYL. Guía del VE.**  
<http://www.vehiculoelctrico.jcyl.es/>



## Abstract

The research is being developed in parallel with ALIS project, a collaboration between Inabensa, the Technical University of Madrid and the University of Málaga, within the challenge of: Smart, sustainable and integrated transport, established in Retos – Colaboración 2015.

The main objective is to generate a working tool whose characteristics are nonexistent today. That need has been identified by the Department of Engineering of the Railway Division of Inabensa.

The tool is going to be based on the interaction between several modules. Some of the modules focused on smart, sustainable and integrated transport which are included in the ALIS project are:

- Location optimization of the substations.
- Optimization of tense of the catenary and the pantograph and catenary interaction.
- Simulation of the electric protection equipment as well as the ground return and stray currents.
- Conditions of the rail system, such as electromagnetic interference, wave quality, electromagnetic compatibility and diseases to humans.
- Optimization of railway electrical system.
- Efficient driving and energy saving.
- Hybrid systems for energy storage.
- Integration of renewable energy supplies in the sector.

## First Stages

### Definition of the problem

Once the main objective has been divided into modules, the challenges to be faced while solving the problem should be known.

By focusing the beginning of research on the behavior of the catenary in their interaction with the pantograph, the first step will be to generate models for the mass and damping factors that have to be taken into consideration.

### Definition of a starting point

Being a project in an early stage of development, the second thing to do is to determine the starting point.

In this case, the first studies that has to be performed are focused on the tense of the catenary.

The next step will be to create a mathematical model of the catenary. Matlab has been used to define the geometry of the wire and the hangers. In order to perform the calculations of the deformation, a finite element method is used, taking the main holder and conductive wires as beam elements and the hangers as elements that do no work when compressed.

## First results

### Catenary deformed according to the load

As soon as the model with the loads has been defined, deformation studies as well as contact studies begin to show the first results. In this case the geometry of the bended wire is obtained so it can be applied over the pantograph.

### Contact forces

The existing contact force between the pantograph and the catenary is one of the results that can be obtained using this model. As it can be seen on the graph, those forces depends on the position of the collecting shoe as it goes through the points where a hanger is set.

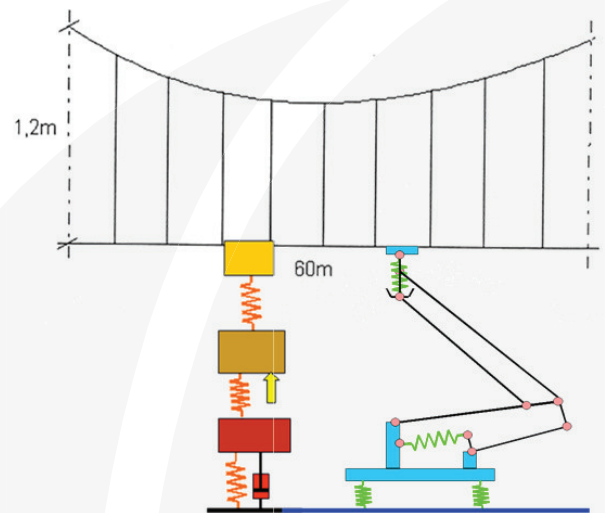
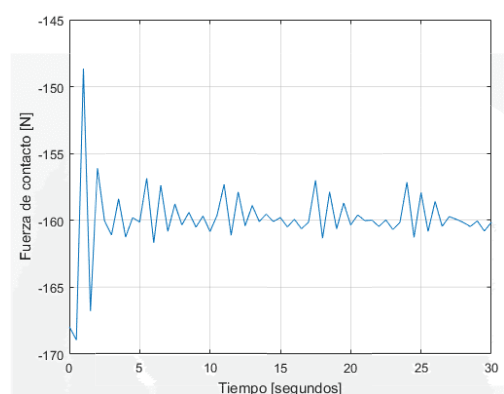
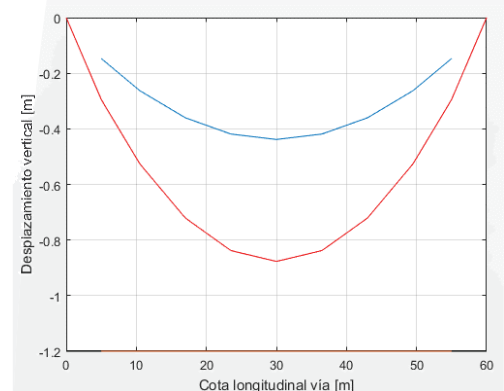


Figura 7. Modelo pantógrafo-catenaria.





# Soil Structure Interaction in Underpasses Structures due to High-speed Trains

<sup>a</sup>Manuel F. Báez Henríquez, Alberto Fraile de Lerma

<sup>a</sup>Depto. Ing. Mecánica, ETSII, UPM(mf.baez@alumnos.upm.es)

## Abstract

A model is proposed to verify the dynamic behavior of underpasses structures in high-speed rails. These structures have been studied in the last few years with models which provide a good insight into the main structure. Those models have been focused in the vertical accelerations of the slab without taking into account the behavior of the walls. The current model focus not only in the vertical acceleration in the slab but also in the horizontal acceleration in the vertical supporting elements. An emission model is used to simulate the trains and is attached to a finite element model of the structure, the results will be compared to on-site measurements which will allow the model fitting in order to obtain a simplified model.

## Introduction

Underpasses structures are subject to vibrations due to the transient dynamic loads originated high-speed trains. The main objective is to obtain a simplified model which allow to know the response in the wall and the slab of the underpass structures. Some other objectives are the auscultation and analysis of results in the railway, sleepers (crosstie), slab, etcetera which will allow to fit the models.

## On-site Measurements and Monitoring Results

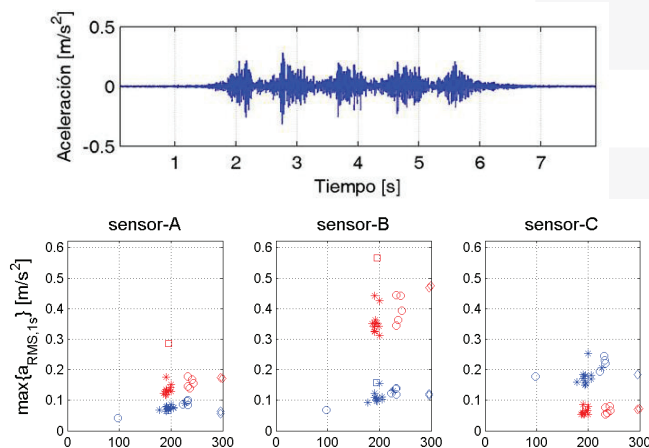
### On-site Measurements

Sensors are used to obtain the acceleration response in the railway, sleepers, slab and the walls. The sensors are located in specific points where the maximum values are expected. Then the signals obtained from the devices are conditioned, digitalized and stored for later analysis and processing.



### Monitoring Results

The time-history series for each sensor are processed in order to obtain the maximum values of acceleration as a function of the location.

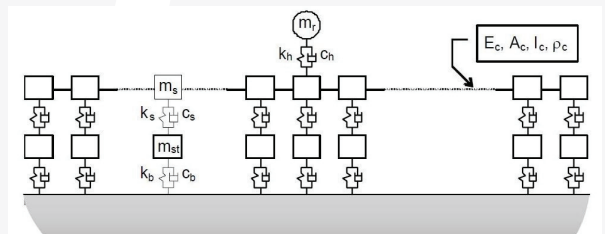


## Modeling

Two models are combined in order to get the response of the structure: an emission model for the actions, and a transmission model for the structure.

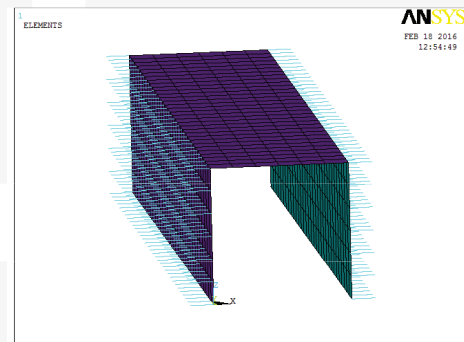
### Emission

The railway is modeled taking into account the non-suspended mass of the vehicle, the roughness of the way, the spring and dampers corresponding to the sleepers, and the track ballast.



### Structure

The structure is modeled using 4-node plate finite elements and Kelvin-Voigt elements for the soil structure interaction.



### Full Model

A "full model" is being developed in MATLAB® which will incorporate the emission model into the structure, this will take into account the changes in the structure due to the movement of the non supported mass (the train) at any step and position and give the insights for a simpler model for the response in the slab and the wall.



## Authors' index

Abánades, Alberto	101
Abbas, Rubén	95
Abou-Assali, Alejandro	164
Acosta, Jessica	162
Aguinaco, Teresa	162
Alarcón, Covadonga	166
Alarcón, Enrique	173, 177
Alba, Fernando	165
Alcázar, Victoria	55, 96
Aledo, David	76
Alonso, Beatriz	47, 48, 49, 50
Alonso, Jesús	4, 10
Alonso, Nicolás	23, 24
Alonso-Álvarez, Jesús	178, 179
Alou, Pedro	19, 21, 22, 23, 36, 73
Alvarado, Biel P.	89
Alvaro-Hermana, Roberto	218
Angulo, Ignacio	131
Aracil, Rafael	88
Arenal, Alberto	148
Arenas, Ana	55, 57
Arenas, María	96
Armuña, Cristina	148
Arroquia, Andrés M.	51
Artiñano, Begoña	114
Artuñedo, Antonio	219
Asensi, Rafael	64, 65, 217
Asensio, César	3, 7, 8, 9, 10
Báez, Manuel F.	223
Ballesteros Sánchez, Luis	143
Bañares, Luis	130
Barredo, Josu	166
Barrera, Eduardo	25, 85
Barrientos, Antonio	18, 41
Barrios, Dolores	169
Bartolomé, José Florindo	56
Belinchón, Julio A.	192
Bellazi, Khalifa	77
Bellón, Irene	183
Beltrán, Freddys	157
Benavent-Climent, Amadeo	206, 207, 209
Benito, Belén	203, 204, 205, 208, 210, 211
Bernabeu, Hugo	157
Bernal, Enrique	85
Borge, Rafael	109, 111, 112, 113, 114, 117
Borović, Uros	24



Bouvier, Yann E.	23
Bravo, Luis A	6
Breñosa, José	88
Bringa, Eduardo	191
Brun, Alessandro	149
Cabrera, Daniel	36
Calvo, Álvaro	222
Cambronero, Luis E.	42
Campoy, Pascual	16, 17
Cano Nogueras, Javier	221
Cansado-Bravo, Pablo	104
Canteli, David	98
Cañadas, Raquel	155
Capel, Francisco	178
Capitán-Herráiz, Álvaro	63
Cara, Javier	173, 174
Cardoso, Jose	124
Caro, Eduardo	174
Carpeño, Antonio	81
Carrio, Adrian	17
Casado, Carmen	47, 48, 49, 50
Casquel, Rafael	33, 37, 78
Castañares, César	82, 86
Castellote, Marta	117
Castro, Emilio	190
Caturla, María José	191
Chacón, Enrique	164, 183
Chen, Yu	98, 123
Ciarapica, Filippo E.	141
Cisneros, Manuel	42
Cobos, José Antonio	73, 97
Conejo, Ramón	39
Cordero, José María	117
Cordovilla, Francisco	129, 132, 133, 134, 135
Correa, Carlos	131, 133
Cotelo, Manuel	198, 199
Cruz, Darío	193
Čučak, Dejana	73
Cuervo, Diana	188
de Andrés, Juan Manuel	111, 114, 119
de Arcas, Guillermo	7, 10, 81, 84
de Blas, Adrián	158, 180
de Blas, Carlos	120
de Castro, Rosa M <sup>a</sup>	216
de la Calle, Bernardo	169
de la Fuente, M <sup>a</sup> del Mar	110
de la Guerra, Eduardo	183
de la Orden, María Ulagares	55, 57, 157, 160
de la Paz, David	111, 112, 113, 114

de la Sota, Candela	109
de la Torre, Eduardo	38, 39, 82, 83, 86
de León, Jorge	80
de Sanctis, Ilaria	141
del Cerro, Jaime	18, 41
del Peso, Isabel	110
Díaz, Andrés	158, 180
Díaz, Ismael	53, 54
Díaz, Javier	134
Díaz, Marcos	126, 127, 128
Díaz, Pablo	130, 163
Diez, Alberto	87
Domínguez, Jesús	129, 132
Domínguez, María Elena	169
Echávarri, Javier	183
Encalada, Patricio	89
Esquembri, Sergio	81, 84, 85
Estaire, Luis	142
Esteban-Cubillo, Antonio	56
Fajardo, Marcelo	181
Fernández Zapico, Guillermo	125
Fernández, Iván	163
Fernández, Javier	177
Fernández, José María	72
Ferre, Manuel	88
Flores-Gutiérrez, José	151
Flores-Márquez, Sandra	151
Fonseca, Carmen	162
Foteinopoulou, Katerina	161
Fraile, Alberto	166, 177, 223
Fraile-Ardanuy, Jesus	218
Francés, Airán	64, 66
Francisco Javier, Sanza	37
Franco Riquelme, José N.	152
Galán, Ramón	89
Galé, David	206, 209
Gallego, Eduardo	197
Gálvez, Gerardo	31, 32
Gamarra, Álvaro	95
García Armada, M. Pilar	47, 48, 49, 50, 51
García, Alejandro	67
García Laso, Ana	144
García, Ana M.	42, 43, 44, 155, 156, 192
García, Antonio	215
García, Gonzalo	88
García, Óscar	26, 64, 66, 67, 72, 73
García-Ballesteros, Juan José	98
García-Beltran, Ángel	129, 131, 132, 133, 134

García-Herranz, Nuria	187, 190
García-Rebollar, Paloma	120
Garoz, David	194
Garzón, David A.	80
Garzón, Mario	80
Garzón, Miguel	134
Gascó, Luis	7, 31
Gaspar-Escribano, Jorge	203, 204, 205, 208, 210, 211
Gatío, Beatriz	114
Geißler, Tobias	101
Gillier, Adèle	35
Gómez-Ferrer, Begoña	193
Gómez-Moreno, Francisco José	114
Gong, Bing	103, 115
González Arrabal, Raquel	163, 196
González, Agustín	136, 198, 199
González, Celina	102, 105
González, César	195
González, Emilio	53, 54
González, Juan	197
Gordillo, Nuria	196
Guarderas, Galo	65
Guo Qing	116
Guzmán, Karen	197
Haber, Rodolfo	219
Haghi, A.	205
Hermanns, Lutz	166, 177
Hermida, Luis F.	9
Hernández, Ana L.	33, 37, 78
Holgado, Miguel	33, 37, 78
Holguín, Fermín A.	74
Huerta, Daniel	124
Huerta, M <sup>a</sup> Consuelo	178, 179
Iglesias, Pablo	39
Izquierdo, Jesús G.	130
Jagdheesh, Radhakrishnan	124
Jaráiz, Daniel	57
Jiménez, Ángel	102, 105
Jiménez, Elvin	61
Jiménez, Gonzalo	189
Jiménez, Javier	34
Jiménez, Lidia	157
Juan, Jesús	145, 173, 174
Kane, Moustapha	109
Karaosman, Hakan	149
Karayiannis, Nikos	161



Laguna, M <sup>a</sup> Fe	33, 37, 78
Lansac, Bruno	78
Laso, Manuel	161
Lauzurica, Sara	40, 98
Lavín, Álvaro	33, 37
Lazarevic, Vladan	26
Le-Garrec, Bruno	194
León, Salvador	160
López Paniagua, Ignacio	102, 105
López, Inmaculada	47
López, Javier	27
López, Juan Manuel	4, 10, 11
López, Máximo	61
López, Sergio	81
López-Alonso, Emma	189
López-Estrada, Luis	181, 182
López-Ramos, Antonio	140
Lorente, Alfredo	197
Lorenzo, Sara	157
Lorenzo, Vicente	57, 157, 162
Losada, José	47, 48, 49, 50, 51
Lu Dang Khoa, Nguyen	87
Lucio, José F.	6
Luengo, David	169
Lumbreras, Julio	109, 111, 114, 117, 118, 146, 147
Maañón, Jesús	27
Maigler, Mavi	33, 37
Marcos Ortiz, Isabel	145
Mármol-Acitores, Gloria	100
Marquez, Andrés	98
Martilli, Alberto	113
Martín, Domingo	144
Martín, Fernando	114
Martin, Jaime	52
Martín-Bragado, Ignacio	195
Martínez Perales, Silvia	145
Martínez, Emilio	117
Martínez, Francisco	220
Martínez, Luis	215
Martínez, Sergio	61, 93, 99, 218
Martínez-Cuevas, Sandra	57, 157, 160, 203, 204, 205, 208, 210, 211
Martínez-Urreaga, Joaquín	55
Martínez-Val, José María	95, 221
Matía, Fernando	89, 219
Mazorra, Javier	109
Mena, Diana	160
Méndez, P.	10
Mendonça, Hugo	99
Menéndez, Guillermo	96
Mínguez Anchuelo, Arcángel	125

Miñano, Rafael	146
Miragliotta, Giovanni	103
Mitra, Swarnava	170
Molina, Álvaro	55, 57, 157
Molina, Jon	163
Molpeceres, Carlos	40, 98, 123
Monclús, Miguel	163
Mora, Javier	39, 83
Morales, Miguel	40, 98, 123
Morales-Alonso, Gustavo	149, 150
Moreno, Ana	146, 147
Moreno, Diego A.	42, 43, 44, 155, 156, 192
Moreno, Félix	76, 79
Moreno, Javier	157
Mota, Santiago Félix	207, 209
Munnik, Frans	196
Muñiz, Maria	112
Muñoz, Alejandro	134
Muñoz, David	98, 123
Muñoz, Juan Manuel	125, 164
Muñoz, Ricardo	95
Muñoz, Santiago	75, 78
Muñoz-Antón, Javier	95
Naffakh, Mohammed	155, 159
Nájera, Jorge	216
Narros, Adolfo	109, 110, 114, 117, 119
Naziris, Antreas	217
Nieto, Julián	84
Nieto, Rafael	102, 105
Núñez, Andrés	42, 43
Ocaña, José Luis	124, 126, 127, 128, 129, 131, 132, 133, 134, 135
Ochoa, Almudena	162
Ochoa, Danny	93
Oliva, Eduardo	198, 199
Oliver, Jesús Ángel	19, 20, 21, 22, 36, 73
Oliveros, Ingrid	61
Ordieres, Joaquin	103, 115, 141, 152, 165, 170, 171
Ortega, Elena	157
Ortiz, Isabel	139, 143
Ospina, Evelyn	49
Pablo-Lerchundi, Iciar	150
Pacios-Álvarez, Antonia	178, 179
Pagán, José A.	87
Panizo Laiz, Miguel	196
Parra-Hidalgo, Jose A.	178, 179
Pavón, Ignacio	4, 5, 6, 8, 9, 10, 11
Pearce, Gillian	35
Peña-Rodríguez, Ovidio	130

Peña-Torres, Dionicio	62
Peral, David	126, 127
Pérez, David	79
Pérez, Javier	111, 114, 118
Perlado, José Manuel	130, 163, 191, 194, 195, 196
Platero, Carlos	68
Porro, Juan Antonio	126, 127, 128
Portilla, Jorge	67, 75, 78
Potti, Irene	78
Prada, Alejandro	130, 191
Prieto López, Roberto	74
Puertas, María Luisa	56
Punjabi, Divesh	50
Quaassdorff, Christina	111, 114
Querol, Xavier	109
Quintero, Sergio Andrés	78
Quirós, Ligia Elena	203, 204, 205, 208, 210, 211
Ramírez, Cristina	165
Ramírez, Jorge	96
Ramos, Juan Carlos	88
Ramos, Pablo	161
Ramos, Regina	71
Ranninger, Carlos	44
Ranninger, José M.	42
Rathnam, Renu Kumar	101
Rebollo, Emilio	67
Recuero, Manuel	31, 32
Ribas, Alicia	211
Riesgo, Teresa	38, 39, 75, 77, 78, 82, 83, 86
Rivas, Víctor	66
Rivera, Antonio	130, 163, 191, 194, 195, 196
Rivera, Javier	215
Roche, Elena	119
Rodríguez Martín, Javier	102, 105
Rodríguez, Alfonso	82, 86
Rodríguez, Encarnación	110, 114, 117, 118, 119
Rodríguez, Enrique	139
Rodríguez, Jaime	216
Rodríguez, Manuel	52, 53, 54
Rodríguez-Monroy, Carlos	62, 63, 100, 104, 120, 140, 151
Rodríguez-Páramo, Ángel	194
Rojas, Javier	36
Roldán, Juan Jesús	18
Romero, Gregorio	35
Rossi, Claudio	41
Rubbia, Carlo	101
Ruiz de Lara, Leonardo	126, 127, 128, 135
Ruiz, Mariano	25, 81, 84, 85
Ruiz-Barajas, Sandra	203, 204, 205, 208, 210, 211



Ruiz-Román, José M.	42
Ruiz-Yherla, Juan Bautista	15
Sabater, Adrián	188
Saiz-López, Alfonso	112, 114
Salinas, Guillermo	21, 22
San Millán, Julio	221
San Millán-Castillo, Roberto	5
Sánchez, Alejandro	183
Sánchez, Carlos	110
Sánchez, Jacobo	179
Sánchez-Cervera, Santiago	187
Sanchez-Lopez, Jose Luis	16
Sánchez-Orgaz, Susana	105
Sánchez-Pascual, Álvaro	88
Sancho, Paula	129, 132
Sansigre, Gabriela	169
Santamaría, Beatriz	33, 37
Santiago, José Antonio	127, 128, 130, 163
Sanz, Ricardo	87
Sanza, Francisco Javier	33, 78
Sapiña, María	117
Sebastián, José María	88
Serrano, Diego	97
Shrouf, Fadi	103
Shuai Chuanmin	116
Silva, Marcelo	19
Solvoll, Anne Marthe	157
Sordo, Fernando	194
Staller, Alejandra	203, 204, 205, 208, 210, 211
Stevanovic, Branislav	21, 22, 27
Stoppel, Leonid	101
Stückrad, Stefan	101
Suriano, Leonardo	38, 86
Tafur, Javier	139
Talayero, Carlos	35
Tejado, Elena	196
Terciado, Carlos	36
Torres, Yolanda	203, 204, 205, 208, 210, 211
Travesí, Jaime	183
Tristán, Edgar	11
Tur, Alejandro	135
Uceda, Javier	64, 65, 66, 217
Valles, Gonzalo	195
Vargas-P., Ana M.	150
Vasić, Miroslav	21, 22, 26, 27, 73, 97
Vedrenne, Michel	118
Vega-Carrillo, Héctor	197

Veganzones, Carlos	94
Velarde, Pedro	136, 198, 199
Viana, Mar	109
Vila, Rafael	193
Villafaña, Oscar	209
Villaverde, Mónica	79
Villazón, Carlos	9
Villena, Carlos	50
Vizán, Antonio	181, 182
Wennberg, Ambiorn	163
Wetzel, Thomas	101
Yagüe, Carlos	114
Yang, Liu	172
Yáñez, Susana	147
Yazdi, Pouye	203, 204, 205, 208, 210, 211
Yousefi, Abouzar	52
Zarei, Mohammad Ebrahim	94
Zarzo, Alejandro	169
Zhao, Sisi	19
Zheng, Xiaochen	171
Zubitur, Iñigo	71



## **Escuela Técnica Superior de Ingenieros Industriales Universidad Politécnica de Madrid**

José Gutiérrez Abascal 2  
28006 Madrid - España  
Tel. 91 336 3060  
[www.industriales.upm.es](http://www.industriales.upm.es)

